VALIDATION OF LEVEL 2 TRMM RAIN PROFILE ALGORITMS

BY INTERCOMPARISON AND HYPOTHESIS TESTING

By

THROY D. HOLLIS

Capt., USAF

1999

Master's Thesis

From

Florida State University

63 Pages

ABSTRACT

The most common method of verifying satellite rain estimates is by comparison with ground 'truth' derived from measurements obtained by raingage networks, ground weather radar, or a combination of the two. However, these types of measurements often have uncertainty magnitudes on the order or greater than the satellite algorithms, motivating the search for alternate approaches. The purpose of this research is to explore a new type of approach for validating the level 2 TRMM facility rain profile algorithms. This is done by an algorithm-to-algorithm intercomparison analysis in the context of physical hypothesis testing.

Seven hypotheses were formed detailing expected performance characteristics of the algorithms. Procedures were developed to test these hypotheses and applied to 48 storms from all ocean basins within the tropical and sub-tropical zones over which TRMM coverage is available ($\sim 35N - 35S$). The testing resulted in five hypotheses verified, one partially verified, and one inconclusive. These findings suggest that the four level 2 TRMM facility profile algorithms are performing in a manner consistent with the underlying physical limitations in the measurements, providing an independent measure of the level 2 algorithms' validity.

REPORT DOCUMENTATION PAGE			Form Approved OMB No. 0704-0188

1. AGENCY USE ONLY (Leave blank)	2. REPORT DATE 17.Feb.00	3. REPORT TYPE AND DATES COVERED THESIS

4. TITLE AND SUBTITLE
VALIDATION OF LEVEL 2 TRMM RAIN PROFILE ALGORITHMS BY INTERCOMPARISON AND HYPOTHESIS TESTING

5. FUNDING NUMBERS

6. AUTHOR(S)
1ST LT HOLLIS THROY D

7. PERFORMING ORGANIZATION NAME(S) AND ADDRESS(ES)
FLORIDA STATE UNIVERSITY

8. PERFORMING ORGANIZATION REPORT NUMBER

9. SPONSORING/MONITORING AGENCY NAME(S) AND ADDRESS(ES)
THE DEPARTMENT OF THE AIR FORCE
AFIT/CIA, BLDG 125
2950 P STREET
WPAFB OH 45433

10. SPONSORING/MONITORING AGENCY REPORT NUMBER
FY00-74

11. SUPPLEMENTARY NOTES

12a. DISTRIBUTION AVAILABILITY STATEMENT
Unlimited distribution
In Accordance With AFI 35-205/AFIT Sup 1

12b. DISTRIBUTION CODE

13. ABSTRACT (Maximum 200 words)

14. SUBJECT TERMS

15. NUMBER OF PAGES
63

16. PRICE CODE

17. SECURITY CLASSIFICATION OF REPORT	18. SECURITY CLASSIFICATION OF THIS PAGE	19. SECURITY CLASSIFICATION OF ABSTRACT	20. LIMITATION OF ABSTRACT

THE FLORIDA STATE UNIVERSITY

COLLEGE OF ARTS AND SCIENCES

VALIDATION OF LEVEL 2 TRMM RAIN PROFILE ALGORITHMS

BY INTERCOMPARISON AND HYPOTHESIS TESTING

By

THROY D. HOLLIS

A thesis submitted to the
Department of Meteorology
in partial fulfillment of the
requirements for the degree of
Masters of Science

Degree Awarded:
Fall Semester, 1999

The members of the Committee approve the thesis of Throy D. Hollis defended on 4 November 1999.

_____

Eric A. Smith
Professor Directing Thesis

_____

T. N. Krishnamurti
Committee Member

.

_____

Henry Fuelberg
Committee Member

ACKNOWLEDGEMENTS

TABLE OF CONTENTS

LIST OF TABLES

LIST OF FIGURES

ABSTRACT

Satellite algorithms are currently the methodology showing most promise for obtaining more accurate global precipitation estimates. However, a general problem with satellite methods is that they do not measure precipitation directly, but through inversion of radiation-rain relationships. Because of this, procedures are needed to verify algorithm-generated results. The most common method of verifying satellite rain estimates is by comparison with ground 'truth' derived from measurements obtained by raingage networks, ground weather radar, or a combination of the two. However, these types of measurements often have uncertainty magnitudes on the order or greater than the satellite algorithms, motivating the search for alternate approaches. The purpose of this research is to explore a new type of approach for validating the level 2 TRMM facility rain profile algorithms. This is done by an algorithm-to-algorithm intercomparison analysis in the context of physical hypothesis testing.

Beginning with the four algorithms' strengths and weaknesses garnered from the physics used to develop the algorithms, seven hypotheses were formed detailing expected performance characteristics of the algorithms. Procedures were developed to test these hypotheses and applied to 48 storms from all ocean basins within the tropical and sub-tropical zones over which TRMM coverage is available (~ 35N – 35S). The testing resulted in five hypotheses verified, one partially verified, and one inconclusive. These

findings suggest that the four level 2 TRMM facility profile algorithms are performing in a manner consistent with the underlying physical limitations in the measurements (or, alternatively, the strengths of the physical assumptions), providing an independent measure of the level 2 algorithms' validity.

CHAPTER 1

INTRODUCTION

Precipitation is one of the most important weather phenomena because the world's population depends on a regulated amount of fresh water. Not enough rainfall leads to drought and occasionally famine, while too much causes flooding. These are only the most obvious impacts of precipitation. The not so obvious impacts stem from the production of latent heat, with three-fourths of the heat energy of the world's atmosphere being generated from the release of latent heating by the condensation-precipitation process (Simpson et al., 1996). Thus, latent heating is the main diabatic factor in the thermodynamic control of the Earth's climate and general circulation.

As important as precipitation is to man's welfare, there are still major problems associated with its measurement. Precipitation is difficult to measure accurately because it does not occur uniformly at area-wide scales. When a rain cell tracks directly over a rain gage measuring station, that measurement is generally not representative of the surrounding area because of the non-ergodic variability in time-space associated with most convective precipitation systems, particularly in the tropics (Seed and Austin, 1990). The same can be said about ground radar, albeit to a lesser degree. However, added to the difficulty of radar is that it is an intrinsically remote sensing measurement; highly susceptible to transmitter-receiver calibration errors. It is also based on beam

1

broadened horizontal signal paths through largely vertically structured rain clouds, often overshooting the main rain layer and generally limited to land areas and coasts (see Smith et al., 1998). Also, since it is unrealistic to deploy rain gauges, radars, or other ground measuring devices to cover the entire Earth's surface, especially over oceans, which make up three-fourths of the global surface, large areas have historically gone without systematic *in situ* measurements. The only viable means to overcome this limitation is through satellite remote sensing.

Besides the purely scientific search for knowledge, there are also real world benefits in improving the measurement of precipitation. One of these is improved weather and climate forecast models. Today's models use different methods for estimating precipitation and the accompanying release of latent heat. Because of this, discrepancies occur between large scale prediction models forced with standardized inputs (Gadgil and Sajani, 1999). However, current methodologies for obtaining vertical latent heating structures from rain profile retrieval algorithms have proved viable (Smith et al., 1992, Tao et al., 1993a, Yang and Smith 1999a-c). Moreover, accurate estimates of precipitation and latent heating used for model initialization have been shown to lead to more accurate forecasts (Hou et al., 1999a-b). Finally, improvements in global precipitation measurment lead to a better physical understanding of important weather-climate phenomena such as the El Niño-Southern Oscillation (ENSO) (Simpson et al., 1988).

Satellites are the technology showing most promise for obtaining more accurate global precipitation measurements. Satellites enable observations of a greater area of the Earth's surface for a sustained period of time than do any other type of measuring

2

platform. Of course, the general problem in using satellite instruments to measure precipitation is that they cannot measure rainfall or rainrate directly, instead requiring the use of some type of inversion scheme involving radiative properties of the atmosphere, and the emission, transport, and attenuation processes of the measured radiative quantities. Much research has gone into precipitation retrieval methods employing optical and infrared imagery since the late 1960's (e.g., Barrett and Martin, 1981), and more recently with passive microwave imagery (e.g., Wilheit et al., 1994; Smith et al., 1998).

Because satellites do not measure rainfall directly, procedures are needed to verify retrieved estimates (see Dodge and Goodman, 1994). The most common method of verifying satellite-retrieved rain estimates is to directly compare to ground validation measurements (ground truth) derived from raingage networks, ground weather radar, or a combination of the two. However, there are well known errors associated with measuring rainfall with raingage networks (Rodriguez-Iturbe and Mejia, 1974; Damant et al., 1983; Bellon and Austin, 1986; Seed and Austin, 1990; and Morrisey, 1991) as well as with ground radar systems (Harrold et al., 1973; Damant et al., 1983; Seed and Austin, 1990; and Smith et al., 1998). In essence, *in situ* methods do not measure "true" rainfall in the strict interpretation of ground truth. Therefore, since there are no 100% reliable *in situ* rainfall measurements that can be used as a benchmark for verifying or calibrating satellite algorithms, alternate methods are welcomed.

The purpose of this research is to explore an alternate approach for satellite rainfall validation. This is done by algorithm-to-algorithm intercomparison in the context of

physical hypothesis testing. The algorithms in question are the four level 2 Tropical Rainfall Measuring Mission (TRMM) facility rain profile algorithms.

On 28 November 1997, the TRMM satellite was launched from the Tanegashima launch range in Japan. The TRMM program is a joint venture between the U.S.'s National Aeronautics and Space Administration (NASA) and Japan's National Space Development Agency (NASDA) (Simpson et al., 1988, 1996). The TRMM satellite is the first Earth-orbiting mission dedicated to studying precipitation and latent heating. As its name implies, the TRMM mission has been designed to measure precipitation over tropical latitudes, actually the latitude zone extending from ~ 38°S to 38°N (TRMM carries scanning instruments in a 35 degree inclined prograde orbit). The mission is also designed to obtain the horizontal, vertical, and temporal distribution of latent heating over the tropics. The tropical regions are important because more than two-thirds of global precipitation occurs there, while diabatic heating associated with precipitation processes strongly controls the large-scale general circulation, tropical waves, and seasonally/intraseasonally modulated weather disturbances.

Notably, tropical convective and stratiform cloud systems are more amenable to accurate satellite rain retrieval than higher latitude winter cyclones and frontal stratiform systems in which baroclinically driven circulations and extensive ice physics complicate the retrieval problem (Simpson et al., 1988). In the tropics, there is also better correlation between high-cold cloud tops and rainrates (Arkin and Meisner, 1987), plus greater progress in microphysical modeling of convective cloud systems (Tao et al., 1993a-b). TRMM's non-sun-synchronous inclined orbit (35 degree prograde) covers the tropics (as well as subtropics), and permits detection and sensing of daily rainfall variations since

any given area is sampled approximately 25–28 times per month at different solar times. Robust sampling is essential in keeping the sampling error low (Shin and North, 1988; Bell et al., 1990). Another feature of the TRMM orbit is its relatively low 350 km altitude, which enables increased resolution for the diffraction-limited TRMM Microwave Imager (TMI), one of the three main rain measuring instruments on the satellite.

The TRMM satellite's instrument package is made up of three primary instruments for rainfall measurement and two additional instruments for lightning detection and cloud-radiation budget measurement (Kummerow et al., 1998). The primary precipitation instruments are the TMI, the Precipitation Radar (PR), and the Visible and Infrared Radiometer System (VIRS). The additional instruments are the Lightning Imaging System (LIS) and the Clouds and Earth's Radiant Energy System (CERES). The focus of this study is on physical algorithms producing rain profiles using the TMI and PR instruments, and their combination.

The TMI is a conically scanning 9-channel microwave radiometer measuring five frequencies, 10.7, 19.4, 21.3, 37, and 85.5 GHz, with horizontal-vertical polarization diversity at all but 21.3 GHz (a water vapor channel which requires only single polarization -- V-pol on TMI). The TMI measures passive microwave radiation emitted by the Earth's surface, water droplets and ice particles in the atmosphere, and the combined effects of gaseous O_2 and H_2O emission, but only after the emitted photons undergo natural scattering and attenuation processes within and throughout the surface and atmospheric media. Such measurements can be used to estimate rainrates because there are physically-sound radiative transfer relationships associated with the

microphysical properties of rain and the upwelling passive microwave radiation leaving the atmosphere. The different frequencies are important for obtaining information on different vertical levels of the atmosphere, associated with the distinct channel weighting function properties in the presence of rain (weighting function denotes the vertical derivative of the cumulative transmittance function at a given frequency). The TMI has a swath of 790 km, the widest scan of the three primary TRMM rain instruments, making it the widest coverage instrument for measuring rain.

The PR instrument is the first ever spaceborne rain radar. It is based on non-coherent aluminum waveguide technology, transmitting at a frequency of 13.8 GHz with a swath width of 220 km. The PR measures the attenuated reflectivity of the transmitted signal to rain hydrometeor targets, to the Earth's surface, and to the ocean's mirror image. This reflectivity (Z) information can be used to construct 3-dimensional renditions of rainrate (R), particularly when the radar is well calibrated and there are representative Z-R relationships on hand. The PR is also important for its ability to measure precipitation over land, where passive microwave imagers traditionally have difficulty because of poor contrast between the generally radiometrically warm precipitation signal and the highly emissive land surface.

Having multiple rain-sensitive instruments on the same satellite platform leads to what may be TRMM's greatest advantage, the possibility for employing combined instrument algorithms. Until TRMM, radar and radiometer techniques have been largely confined to single instrument methodologies. Using algorithms that combine measurements from more than one instrument sensitive to different microphysical

properties allows compensation for some of the individual weaknesses of the single instrument algorithms, theoretically resulting in more accurate measurements of rainfall. The organization of this paper is to first describe the four level 2 TRMM facility profile algorithms being intercompared (section 2), then discuss how the intercomparison datasets were created (section 3). The paper then describes the methodology used to compare the algorithms to each other in the context of the underlying hypotheses (section 4), followed by an explanation of the results of the intercomparisons and their interpretation in the context of hypothesis testing (section 5). Finally, succinct conclusions are offered (section 6). The overall finding is that the four level 2 TRMM facility profile algorithms are performing in a manner consistent with the physical limitations of the measurements, and the physical assumptions underlying the algorithm designs. This result provides an independent validity check on level 2 TRMM profile algorithms and greater assurance that modeling and diagnostic studies of the Earth's climate and general circulation will advance.

CHAPTER 2

DESCRIPTION OF TRMM FACILITY ALGORITHMS

The main dataset used for this study comes from the four level 2 TRMM facility profile algorithms as described in Smith et al. (1999b). Each algorithm produces vertically distributed rain profiles. Two of the algorithms are single instrument algorithms, while the other two are combined algorithms.

The nomenclature used to identify the algorithms is the same used by the TRMM science teams and described in Simpson and Kummerow (1996). The nomenclature divides the algorithms into levels and categories according to the type of product generated. This study uses four TRMM facility types of products: products 1b, 2a, 2b, and 2x. Level 1-Type b algorithms produce calibrated radiation quantities at full resolution in Earth-located orbit swath format. Level 2-Type a algorithms produce geophysical parameters (e.g., rainrates) at full resolution in Earth-located orbit swath format. Level 2-Type b algorithms produce geophysical parameters with some type of averaging process applied, also in Earth-located orbit swath format. Finally, Level 2-Type x algorithms are advanced experimental versions of 2b algorithms, being readied for replacement of official 2b versions.

2.1 TMI Brightness Temperatures (1b11)

The output of the 1b11 algorithm consists of brightness temperatures (T_Bs) for all channels of TMI. This algorithm is not part of the intercomparison per se, but its data are used in stratifying the results from the four level 2 rainrate algorithms. Specifically, T_Bs from the 10.7 and 85 GHz vertical channels are used in the study.

2.2 TMI Profile Algorithm (2a12)

The TMI Profile Algorithm (2a12) is a single instrument algorithm. The methodology used in this algorithm is based upon the work of Kummerow et al. (1996), where many realizations of the Goddard Cumulus Ensemble model (Tao and Simpson, 1993) and the University of Wisconsin Nonhydrostatic Modeling System (UW-NMS) (Tripoli, 1992a-b; Panegrossi et al., 1998) are used to establish a set of probability density functions of distinct rainfall profiles. Upwelling T_Bs are obtained from the cloud model profiles by using a forward 3-dimensional radiative transfer model. The modeled T_Bs are then compared to the measured T_Bs to determine a metric of agreement. By weighting profiles from the *a priori* probability density function according to their deviation from the observed T_Bs (Bayesian approach), iterative radiative transfer calculations are avoided, making this technique computationally fast compared to traditional iterative inverse solutions. This technique does not work well when the database of possible cloud structures is not sufficiently populated -- then, an iterative optimization-based technique developed by Smith et al. (1994a-b, 1995a) is more appropriate. However, the current TRMM cloud model database is sufficiently large to negate the need for iterative methods.

One of the 2a12 algorithm's strengths is that it is an attenuation type solution, i.e., the relationship between radiance (or T$_B$) and drop size goes according to D^4 instead of a radar backscatter reflectivity's D^6 type dependence (D representing the diameter of idealized spherical drop). This reduces the sensitivity of the retrieved rainrates to indeterminate vagaries in the drop size distribution (DSD) function. It also uses four polarized frequencies, which provide eight attenuation constraints, as well as a ninth constraint provided by the 21.3 GHz V-pol measurement. Another strength is the presence of the 10.7 GHz channels (~2.8 cm), which provide total liquid water path (LWP) estimates since most rain drops are Rayleigh with respect to X-band wavelengths. One of 2a12's biggest weaknesses is its broad weighting functions, which limit vertical resolution. Another potential weakness is 2a12's dependence on the cloud models' renditions of vertical hydrometeor structure. This algorithm also has the lowest spatial resolution, which leads to greater sensitivity to heterogeneous beam filling. Moreover, any purely passive microwave-based algorithm has difficulty obtaining measurements over land because of the aforementioned contrast problem. Finally, the 2a12 algorithm is the most affected by upper cloud ice loading, particularly at higher frequencies (37 and 85 GHz), while the 2nd lowest frequency 19 GHz measurements are subject to black body saturation at higher rainrates.

2.3 PR Profile Algorithm (2a25)

The second single instrument algorithm is 2a25, the PR profile algorithm, a hybrid method similar to the scheme described in Iguchi and Meneghini (1994). This method uses the radar reflectivity (Z) vector to produce a vertical profile of rain. However, in order to get accurate results, it is essential that the path integrated attenuation (PIA) is

known. To do this, a Hitschfeld-Bordan (1954) solution is used in a first step to accumulate attenuation in a top-down sequence, followed by application of the surface reference technique (SRT) to provide correction guidance across the retrieved vertical rainrate vector according to the difference between the Hitschfeld-Bordan PIA and the SRT-derived PIA (see Meneghini et al., 1983 for a discussion of the SRT method). The Hitschfeld-Bordan solution requires a consistent pair of Z-R and κ-R functions, i.e., $Z = aR^b$ and $κ = αR^β$, where Z is radar reflectivity factor, κ is attenuation, R is rainrate, and a, b, α, β are constants. For the SRT, the surface return from a rain-filled path is compared to that from a climatological rain-free path created by compositing all prior cloud-free pixels from the start of the mission up to the present into a background climatology.

The strengths of 2a25 are its use of range-gated returns, which results in highly resolved vertical structure, and its overall sensitivity to rain detection (~17 dBZ). The greatest weakness in using the SRT scheme is the assumption that the differences between two surface returns are caused only by atmospheric path attenuation, and not dissimilar surface boundary conditions. In reality, surface reflectivity depends on the roughness of the surface due to wind and internal waves over ocean, and seasonally varying biophysical processes over land. The greatest weakness in the measurement itself is that it is a backscatter quantity, proportional to the 6th power of raindrop diameter, and thus sensitive to variant properties of the DSD. Two other potential measurement weaknesses intrinsic to the 2a25 algorithm are its sensitivity to the accuracy of the PR calibration, which may contain residual systematic errors, and severe

11

attenuation at high rainrates which is not accurately retrieved either from integrating the Hitschfeld-Bordan scheme downward or from application of the SRT scheme.

2.4 Day-1 Combined Profile Algorithm (2b31)

Algorithm 2b31 is the first of the two TRMM facility combined algorithms and has been described in Smith et al. (1995b) and Haddad et al. (1997). This algorithm is derived from algorithm 2a25, in which the SRT is used to constrain the Hitschfeld-Bordan solution. However, the 2b31 algorithm is implemented in Bayesian form and uses the vertical-horizontal 10.7 GHz T_Bs from the TMI to estimate 13.8 GHz PIA, thus providing a 2nd PIA constraint beyond the SRT constraint. Radiative transfer calculations demonstrate the viability of using 10.7 GHz T_Bs to determine 13.8 GHz PIAs (Smith et al., 1997). Although this algorithm uses measurements from two instruments, and thus is a genuine combined algorithm, the 10.7 GHz generated 13.8 GHz PIA is used only as a solution constraint provided by a Bayesian equivalent of 2a25, and is thus referred to as a "conservative" combined algorithm.

This algorithm has the same strengths of 2a25, plus an improved PIA constraint derived from the 10.7 GHz T_Bs. Its weaknesses are residual calibration offset and some D^6 sensitivity inherent to the use of backscatter measurements.

2.5 Tall Vector Combined Profile Algorithm (2x31)

The fourth algorithm used in the intercomparison is 2x31, which is a fully combined algorithm referred to as a "tall vector" algorithm. As described in Smith et al (1999a) and Farrar et al. (1999), a tall vector algorithm is an extension of a passive microwave-based inversion scheme based on cloud modeling. For example, the Smith et al. (1994a) SSM/I algorithm, which used hydrometeor profiles from the UW-NMS cloud

model as input into a forward radiative transfer model to produce T_B profiles matched to measured T_B profiles, was the kernel algorithm for the tall vector algorithm described in Farrar et al. (1997). The difference for 2x31 is that the TMI measurements are augmented with reflectivities from the PR at range gates throughout the rain column above and below where the weighting functions of the different radiometer channels peak. This concatenation of radar reflectivities with TMI T_Bs creates what is known as a "tall vector" in an inversion framework, and by giving the radar and passive radiometer measurements equal leverage in an inversion solution, it is theoretically anticipated that this algorithm minimizes the rainrate retrieval uncertainty. In its TRMM implementation, the 2x31 algorithm has similarities to 2b31 in that it is formulated in Bayesian form, negating the need for computationally intensive radiative transfer iterations (Ziad Haddad, NASA/Jet Propulsion Laboratory, 1999, personal communication).

This algorithm shares the strengths of both 2a12 and 2a25 with fewer weaknesses. The weaknesses include sensitivity to any residual calibration offset in the PR and physical inconsistencies between the passive RTE model and the active (radiatively pulsed) RTE model. However, the combined RTE model of Smith et al. (1999a) eliminates the latter problem. It would be anticipated that 2x31 retains some uncertainty due to the PR reflectivity's D^6 sensitivity, but not to the same degree as 2a25 and 2b31 because the attenuation relationships for the entire set of TMI frequencies partially mitigate that sensitivity.

2.6 Algorithm Strengths and Weaknesses

The broad weighting functions of 2a12 limit the vertical resolution of this algorithm, while 2a25 benefits from the PR's range-gated estimates, providing narrower

"effective" weighting functions and much improved vertical resolution, a strength also shared by 2b31 and 2x31. Algorithm 2a12 also has the lowest spatial resolution, which makes it more susceptible to heterogeneous beam filling effects than other algorithms. Moreover, the higher vertical and horizontal resolution provided by the PR give the 2a25, 2b31, and 2x31 algorithms better rain detection sensitivity than the 2a12 algorithm.

On the other hand, the PR measurements are burdened by D^6 sensitivity in association with variant DSD fluctuations, whereas the TMI's attenuation type measurements contain only D^4 sensitivity. Since 2a25 and 2b31 are most dependent on the PR measurements, this increased sensitivity to the DSD is expected to cause greater rainrate uncertainties than with 2a12 and 2x31 at the higher rain intensities. Note, 2x31 is also dependent on PR measurements, but not to the degree of 2a25 and 2b31. Therefore, it is expected to see 2x31 rainrate uncertainties increase at larger rainrates beyond those of 2a12, but not as great as those of 2a25 or 2b31. Higher rain intensities will also cause saturation at TMI frequencies from 19 GHz on up. This will temporize the constraints offered by those frequencies on the 2a12 and 2x31 algorithms. Since this means 2x31 will become more dependent on the TMI Rayleigh frequency (10.7 GHz), similar in a fashion to algorithm 2b31, 2x31 rain estimates are expected to agree more with the 2b31 estimates at the highest rainrates.

Another problem at higher rainrates is attenuation of the PR signal. Radar rain estimates at attenuating frequencies are very dependent on an accurate estimation of PIA. The 2a25 relies ultimately on the SRT-derived attenuation constraint that is not as precise as 2b31's attenuation constraint derived from TMI 10.7 GHz T_Bs (Smith et al., 1997), meaning that 2a25's rainrates are expected to contain a further source of uncertainty

14

during intense rain. Finally, 2a12 is more dependent on TMI's higher frequencies than the two combined algorithms, which means 2a12 is most sensitive to upper cloud ice loading.

Being able to identify the strengths and weaknesses of physical algorithms in *a priori* fashion, as discussed above, is the cornerstone of this study. The strengths and weaknesses are expected to yield algorithms performing in predictable patterns in relationship to other physical algorithms. If hypotheses can be drawn and tests developed that underscore these patterns, then conclusions can be drawn about a given algorithm's performance with respect to its expected performance. Table 1 summarizes the strengths and weakness of the four level 2 profile algorithms as the basis for postulating a set of well-founded hypotheses.

Table 1: Known strengths and weaknesses of TRMM facility rain profile algorithms.

Algorithms	Strengths	Weaknesses
2a12	Attenuation type measurement (scattering signal in forward diffraction peak)	Broad weighting functions
	4 polarized frequencies provide 8 attenuation constraints	Ice loading decreases sensitivity to liquid rain
	10.7 GHz channel gives total LWP with little D^6 sensitivity	Retrieval of vertical structure tied to cloud model
		Saturation at frequencies ε 19 GHz
		Heterogeneous beam filling
2a25	Narrow weighting functions (range-gated)	Residual calibration offset
	Rain detection sensitivity	D^6 sensitivity
		SRT-derived attenuation constraint
		Severe attenuation for large rainrates
2b31	All advantages of 2a25	Residual calibration offset
	PIA constraint derived from 10.7 GHz TB	D^6 sensitivity
2x31	All advantages of 2a12 and 2a25	Residual calibration offset
		Physical inconsistencies between passive (steady state) RTE model and active (radiatively pulsed) RTE model
		Some D^6 sensitivity
		Loss of constraints due to saturation of higher TMI frequencies

CHAPTER 3

DISCUSSION OF DATASETS

In order to compare the algorithms, level 2 retrievals from a number of TRMM overpasses were partitioned into small sectors within major precipitation systems. This section discusses how these data subsets were created. There are three different sizes of datasets used for this analysis. The terms used to describe the three sizes are orbit swath, storm region, and storm feature. An orbit swath contains retrievals from one algorithm for one full overpass of the TRMM satellite. A storm region is a subset of an orbit swath. It is made up of all data in a rectangular "box" containing one specific storm of interest. [Note a "box" is defined by two latitude-longitude pairs, i.e., minimum and maximum lat/lon limits, and contains all orbit swath data from pixels within the limits. Also note that storm regions are intrinsically variable in size.] A storm feature is a subset of a storm region. It is created by all data in a square "box" containing only a specific storm feature. All storm features are approximately the same size, and their averaged rainrates make up data points used in much of the intercomparison analysis.

3.1 Creating Datasets

The first step in obtaining the storm data consisted of viewing browse imagery available from the TRMM Science Data and Information System (TSDIS). The browse images consist of multiple orbit swaths, showing the entire coverage of the TRMM

satellite for one full day. When a storm of interest was located on a browse image, the date and time for the storm were noted. This information was then used to access specific orbit swath files containing results from the four algorithms being compared, as well as the 1b11 T_B files.

After orbit swath data files were received, they were visually analyzed using the TSDIS orbit viewer. The orbit viewer provides latitude-longitude coordinates of individual pixels. These coordinates were used to create the minimum-maximum latitude/longitude pairs for the individual storm regions and storm features.

Once the latitude/longitude pairs for each storm region were obtained, they were used to create five files for each storm of interest, one for each of the level 2 algorithms being compared, and one for the TMI T_B data (1b11). Finally, the same process was used to create storm feature files. Six files for each storm feature were produced, one file for each of the four level 2 algorithms, one for the vertical 10.7 GHz T_Bs from 1b11, and one for the vertical 85 GHz T_Bs from 1b11.

3.2 Discussion of Storm Features

The final storm features were all boxes of 0.3° latitude by 0.3° longitude, or approximately 30 x 30 km. The features were made as small as possible to increase resolution, but kept large enough to exceed the spatial resolution of the 10.7 GHz measurements. [The instantaneous FOVs of the 10.7 GHz TMI channels are ~36 km CT x 60 km DT, with effective FOVs of ~9 km CT x 60 km DT.] Only ocean storms were selected, to avoid complex uncertainty problems associated with measuring rainfall over land using passive microwave techniques. From all ocean regions covered by the TRMM satellite during the period 8 October 1998 to 31 October 1998, 49 total storms were

18

selected: 12 tropical storm/hurricanes, 14 inter-tropical convergence zone/southern Pacific convergence zone (ITCZ/SPCZ) segments, and 22 extratropical cyclones/ fronts (see Tables 2 and 3 in the appendix). When categorizing storms into individual features, care was taken to select areas covering the full range of rain intensity, from lightest to heaviest rainrate. The final number of features was 398: 101 from tropical storms, 119 from large scale convergence zones, and 178 from extratropical storms (see Table 4 in the appendix).

A frequency distribution of the storm feature rainrates, based on composite rainrates from the four algorithms, is shown in Figure 1. [Note composite rainrates are obtained by taking the mean value of four separate algorithm results.] The rainrate histogram peaks at 4 mm hr^{-1} with a population of 54. At 10 mm hr^{-1}, the populations are approaching 10, and by 15 mm hr^{-1}, populations are at or below 3.
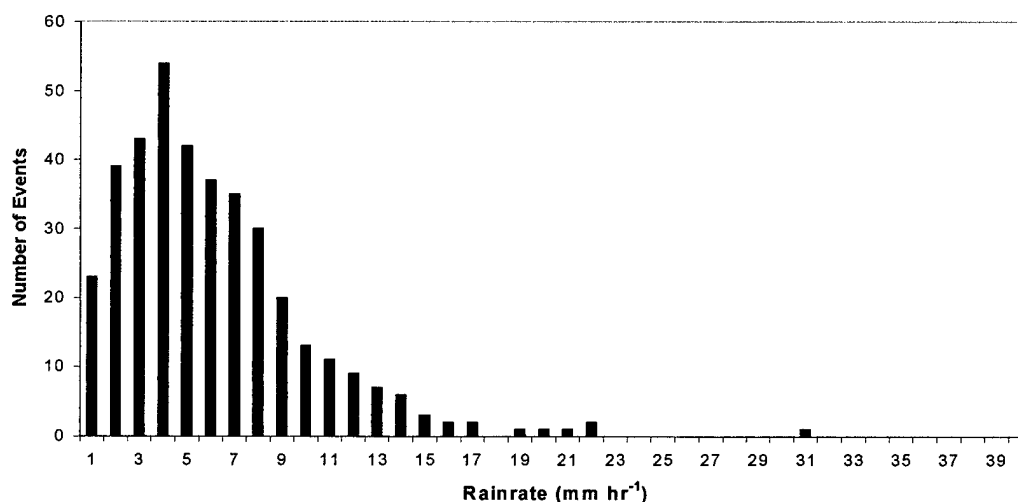
Figure 1: Frequency distribution of feature-averaged composite rainrates.

CHAPTER 4

METHODOLOGY

Any new rain measuring algorithm or measurement device is expected to be tested against conventional ground measurements; thus, research along these lines is being done for TRMM as well. However, this study adopts a different philosophy motivated by the fact that long standing uncertainties in ground verification data translate directly to questions about the validity of the standard verification process. All four of the algorithms being compared are physically based. After designing hypotheses concerning how individual algorithms should perform based on the physical nature of the measurements and the apropos physical assumptions used in the algorithms, we test the hypotheses to see how well the algorithms actually perform against one another in the context of their anticipated performance. Seven hypotheses have been developed and are explained below, along with procedures used to test them. Only pixels with rainrates greater than or equal to 0.01 mm hr^{-1} were used in testing the hypotheses, except for Hypothesis 3. This was done to eliminate the uncertainty associated with the detection of very low rainrates.

4.1 Hypothesis 1: Effect of Ice Loading

The first hypothesis is based on the fact that the 2a12 algorithm solution uses measurements at the higher TMI frequencies, which are, in turn, most influenced by ice

loading. Because of this, surface rainrate differences between 2a12 and the other PR-based algorithms are expected to increase as ice loading increases. To test the hypothesis, the averaged vertical 85 GHz T_Bs (85 GHz being the most sensitive TMI frequency with respect to ice loading) and the averaged surface rainrates from each algorithm for each individual storm feature were compared by graphing the rainrates against the T_Bs (Figure 2). Because of this, as the T_Bs decrease, the 2a12 surface rainrates should diverge from the rainrate graphs of the other algorithms.

Before graphing, the data were averaged in 10°C bins with bin values assigned to the middle of intervals. For example, the first interval is from 280-270 K with an assigned bin value of 275 K. Also, the intervals were overlapped to provide smoothing. For example, the second interval is from 275-285 K with the bin value assigned to 280 K. Besides smoothing, data averaging ensures the data points are spaced evenly and that there is only one value assigned to each bin.

4.2 Hypothesis 2: Radar D^6 Effect

The amount of power back-scattered to a radar by a radar beam intersecting with rain particles is given as $P = (C\ D^6)/r^2$, where P is power, D is diameter of particles summed over a unit volume, r is range, and C is a constant derived from various measurable characteristics of the radar and of the dielectric constant of the rain particles (Harrold et al., 1973). This demonstrates why the received power at a radar is dependent upon the size of the raindrops, varying by D^6. This is known as the D^6 effect. Because of the D^6 effect, radar measurements are affected more by drop size than passive microwave radiometer measurements. Recall the latter is an attenuation type

21

measurement proportional to D^4 and thus less sensitive to indeterminate fluctuations in the underlying DSD functions. Therefore, as storm rainrates increase, signifying larger raindrop sizes, the algorithms most dependent on the PR, i.e., 2a25 and 2b31, should exhibit the largest deviations in rainrate relative to the others. Since the 2x31 algorithm is also dependent on PR input, it should also be affected by the D^6 effect and deviate from the remaining algorithms (i.e., specifically 2a12) at higher rainrates. However, 2x31 should not deviate as much as 2a25 or 2b31 (particularly at intermediate rainrates), because it has a greater degree of attenuation constraint than 2b31, as offered by the "tall vector" approach.

To test this hypothesis, the averaged surface rainrates from each algorithm for each storm feature were obtained, as were the composite surface rainrates for each storm feature. The results were then placed in order of their composite surface rainrate value and binned using the same procedure described in section 4.1, but at 2 mm hr^{-1} intervals with the overlap between intervals set at 1 mm hr^{-1}. The results were then graphed with the algorithm-averaged rainrates being a function of the composite rainrates (diagram not shown). As the composite rainrates increased, the graphs of the 2a25 and 2b31 algorithms were expected to deviate from the graphs of the other two algorithms due to the increased number and size distribution dispersion of raindrops. However, the results of this test were inconclusive because too few samples of high intensity rainrates were used, which is most important for a satisfactory resolution of this test.

In order to get a conclusive result for Hypothesis 2, the data population of the high intensity rainrates had to be increased. To do so, individual pixel values were used.

Using the pixel data in the storm features' files, the first step was to obtain 2a12 surface rainrates pixel by pixel. [The 2a12 algorithm was used as a starting point because it has the lowest resolution, and thus fewer pixels per unit area.] If a surface rainrate was greater than 5 mm hr^{-1}, the nearest 2a25 pixel was located. Once the closest 2a25 pixel was found, it was tested to ensure that the combined difference between the latitudes and longitudes of the two pixels was within 0.03 degrees. If the pixel passed the test, the same latitude-longitude pair was used to select the 2b31 and 2x31 pixels. After finding all pixels obeying the search criteria, the composite algorithm value was calculated. If a composite rainrate was above 8 mm hr^{-1}, the pixel value was added to the averaged storm feature value distribution obtained earlier. This increased the number of values to over 1000, all at the higher rainrates where they were needed.

Once the larger dataset was obtained, the individual algorithm rainrates were again plotted against the composite rainrates (Figure 3), but using a discrete binning procedure, not an overlapping one. From 0 to 16 mm hr^{-1}, the interval was 1 mm hr^{-1}; from 15 to 22 mm hr^{-1}, 2 mm hr^{-1}; and finally above that, the interval was changed to maintain an adequate population of data in a given interval.

4.3 Hypothesis 3: TMI and PR Rain Detection Agreement

As rainrate increases, the detection agreement skill score between 2a12 and 2a25 would be expected to increase, since 2a12 suffers greatest from light rain detection capability. Since the 2a25 algorithm outputs approximately three times the number of pixels per feature as does the 2a12 algorithm, because of its higher resolution, the first step in testing this assumption was to make sure that pixels being tested were from the

23

same location. The 2a12 pixel latitudes and longitudes were obtained first. Next, a 2a12 storm feature was searched for any 2a25 pixel that was within 0.01° latitude and 0.05° longitude. These non-identical values were used because the TMI footprint is larger across the path of a swath than along its path (related to its conical scan pattern), while a PR footprint's dimensions are nearly equivalent in both directions except at extreme scan angles. This allowed for more exact latitude measurements. The 0.05° longitude difference allowed room for location uncertainty, but still kept the 2a25 pixels close to the center of the 2a12 pixel.

Once the co-located pixels were selected, they were both tested for rain/no rain. The results were placed in contingency table bins, three bins for each 0.01 mm hr^{-1} interval up to 20 mm hr^{-1}. The three bins, B1, B2, and B3, represent Yes-No, No-Yes, and Yes-Yes. The bin No-No was not allowed because the pixel selection was made on the basis that one of the algorithms had to include rain. The agreement skill score for each rainrate was then calculated by dividing the number of times both algorithms detected rain, B3, by the total number of times either algorithm detected rain, i.e., B3/(B1+B2+B3). The agreement skill scores were then graphed as a function of rainrate (Figure 4).

4.4 Hypothesis 4: Vertical Structure Differences

The vertical structure differences between the 2a12 algorithm and the other algorithms are expected to be larger than the differences between the other algorithms and themselves, due to the TMI's lack of vertical resolution. The testing of this hypothesis begins by calculating the average rainrate from each algorithm for every level

of each feature, as well as the composite surface rainrate for each feature. Considering the results of the distribution of the composite surface rainrates, three categories of rainfall with approximately the same population were established. The categories are light (0 mm hr^{-1} < R ≤ 4 mm hr^{-1}), medium (4 mm hr^{-1} < R ≤ 9 mm hr^{-1}), and heavy (9 mm hr^{-1} <R). The feature-averaged rainrates are then grouped into the three rain categories and the mean rainrates for each algorithm for each height category are calculated. Finally, these height averaged rainrates are graphed against the composite surface rainrate (diagram not shown).

The 2a12 algorithm would be expected to indicate the largest difference between itself and the other algorithms. However, for this first test the results are inconclusive. The 2a12 values are indeed larger at every level, but the Version 1 2a12 rainrate estimates are known to be approximately 20% larger on a systematic basis than the conservative level 3 reference algorithm 3a11, related to a deficiency in how the 10.7 GHz channels were employed (see Smith et al., 1999b). [This deficiency has been corrected in the Version 2 2a12 estimates for which reprocessed rainrates will be completed in the year 2000.] Otherwise, the diagram shows no significant indication of vertical structure differences besides magnitude. Therefore, a different test was needed for validating or invalidating the hypothesis.

In re-examining the hypothesis, the issue of how TMI's lack of vertical resolution affects 2a12 results was considered in more detail. The peak values of any TMI channel weighting function extend over a much greater depth of atmosphere than does any individual PR range-gated return (see Muganai et al., 1990). Also, the TMI has fewer channels than the PR has range gates. These two characteristics should lead to a relative

25

vertical smoothing effect in the 2a12 retrievals, resulting in smaller differences between the vertical levels in the 2a12 algorithm than between vertical levels in the other algorithms using range-gated measurements.

To test the refined hypothesis, the algorithm-averaged rainrates for each level and each storm feature were calculated. Then the coefficient of variation for each algorithm's rainrate with height was calculated. [The coefficient of variation, which is standard deviation divided by sample mean, eliminates the effect of magnitude bias among the algorithms.] Once the coefficient of variation from each algorithm for each storm feature was obtained, a composite coefficient of variation was calculated using the mean of the four individual algorithm coefficients of variation. Finally, the algorithm coefficients of variation with height were graphed as functions of the composite coefficient of variation (Figure 5). According to the hypothesis, as the composite coefficient of variation increases, the 2a12 algorithm should exhibit the smallest increase.

4.5 Hypothesis 5: Attenuation Effect

Because of liquid water attenuation, which influences radar estimates more than TMI estimates when 10.7 GHz information is used, the differences between the 2a25 algorithm and the other algorithms are expected to increase at a given rain layer depth as the 10.7 GHz T_B increases (assuming heavy ice loading is not present). To test this hypothesis, storm features were first limited to those having an 85 GHz T_B of greater than 240 K to ensure no heavy ice loading (the cutoff was determined from results given in Figure 2). The averaged rainrates from each algorithm for each layer of the feature and the averaged vertical 10.7 GHz T_B for each feature were then calculated. Finally,

graphs for each layer with the averaged rainrate being a function of the 10.7 GHz T_B were created (Figure 6).

The 10.7 GHz T_Bs are proportional to the path integrated liquid water content of a column because the 10.7 GHz frequency is nearly Rayleigh for the characteristic DSD at even heavy rainrates. As the 10.7 GHz T_B increases and the distance the radar beam must travel increases (the lower the range gate, the further the distance), then the differences between the 2a25 algorithm and the other algorithms would be expected to increase.

4.6 Hypothesis 6: Saturation of Higher TMI Frequencies

As rainrate increases, the higher TMI frequencies would be expected to saturate, making less contribution to the solution of the 2x31 algorithm. This would cause 2x31 to become mostly dependent on the 10.7 GHz frequency. Since 2b31 is only dependent on the 10.7 GHz measurement from TMI, the agreement between the rainrate estimations of the two combined algorithms would be expected to increase as rainrate increases. To test the hypothesis, the averaged surface rainrates of the two algorithms were graphed as a function of a "restricted" composite surface rainrate as seen in Figure 7. The "restricted" composite was created by calculating the mean of just the 2b31 and 2x31 averaged surface rainrates. If Hypothesis 6 is valid, the surface rainrates of the 2b31 and 2x31 algorithms will converge as the "restricted" composite surface rainrate increases. The difficulty here is that the effect of Hypothesis 2 is also at work on the relative 2b31-2x31 behavior, thus requiring special attention (see section 5.6 below).

4.7 Hypothesis 7: Beam Filling Effects

Because the TMI is a diffraction limited measurement, its various channels have broader beam widths than the PR. Thus, the 2a12 algorithm is expected to be more sensitive to beam filling heterogeneities. Beam filling heterogeneity occurs when the atmospheric volume being sensed is occupied with non-uniform rainrates and possibly sub-pixel rain-free areas. In this instance, all the different rainrates within the volume of a pixel being sensed are blended together radiometrically, causing inaccuracies in the estimated rainrates since T_B-rainrate relationships are inherently nonlinear. Therefore, since the TMI has the greatest beam widths, there is a greater chance that it will encounter non-uniform precipitation in its measurements.

The storm features used to test this hypothesis were limited to those with 85 GHz T_Bs greater than 240 K to ensure there was low ice loading, just as was done when testing Hypothesis 5. The averaged surface rainrates from each algorithm for each feature were then calculated, as were the variances of the 2a25 algorithm surface rainrates across each feature. The data were then averaged, with the value being assigned to the largest whole number in a variance interval. From 0 to 20 mm^2 hr^{-2} the interval was 5 mm^2 hr^{-2}, while above that point the intervals were selected to maintain an adequate sampling in each interval. After averaging, the results were graphed with the averaged surface rainrates being a function of the 2a25 variance (Figure 8). As variance increases, rainrates for the 2a12 algorithm are expected to diverge from those of the other algorithms.

CHAPTER 5

RESULTS AND INTERPRETATION

5.1 Test of Hypothesis 1

Hypothesis 1 states that the 2a12 algorithm would be most affected by ice loading, since it is the algorithm most dependent on the higher TMI frequencies, which are most sensitive to the volume extinction of ice. Since 85 GHz T_Bs represent the highest TMI frequency, they are necessarily the most sensitive measurements with respect to ice loading. Therefore to test Hypothesis 1, the averaged surface rainrate from each algorithm was graphed as a function of the averaged 85 GHz V-pol T_B as shown in Figure 2.

At the higher 85 GHz T_Bs (low ice loading) all four algorithms show good agreement, with largest differences of about 1.6°C at 250 K. Around 250 K is also where the four algorithms begin to separate. The 2a12 algorithm shows the largest increase, growing by 217% between 250 K and 205 K. The 2x31 algorithm shows the smallest increase, growing by only 127% over the same T_B interval. The other two algorithms, 2a25 and 2b31, maintain good agreement between each other throughout the range of the graph, increasing by ~188%. Therefore the 2a12 algorithm does show a greater change in rainrate with decrease in 85 GHz T_B than any of the other 3 algorithms, confirming that Hypothesis 1 is valid.
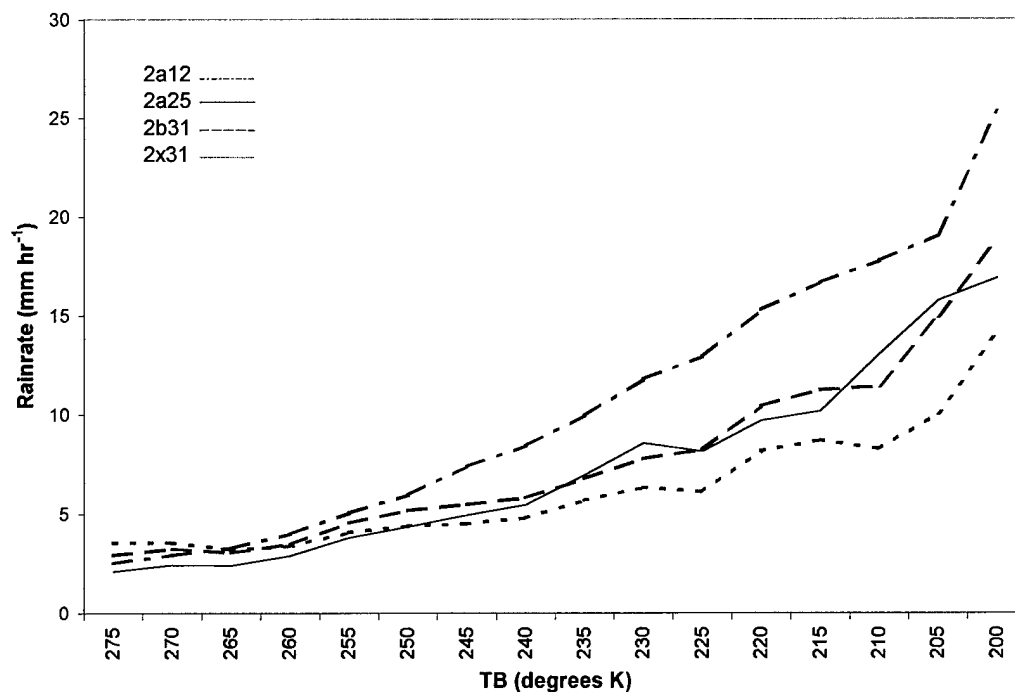
Figure 2: Algorithm-averaged rainrates vs averaged vertical 85-GHz brightness temperatures.

5.2 Test of Hypothesis 2

Because of the D^6 effect in radar measurements, the algorithms most dependent on PR data will show the largest increases in rainrate difference as storm intensity and concomitant rainrate increase. This was the concept expressed in Hypothesis 2. To test the hypothesis, the algorithm averaged surface rainrates were graphed as functions of composite surface rainrate (Figure 3). There is not as much agreement evident in this diagram as there was in Figure 2. The plot of the 2a12 algorithm separates from the others at 3 mm hr^{-1} after only three data bins. The 2x31 plot begins to diverge from the other two algorithms 3 bins later at 6 mm hr^{-1}. The 2a25 and 2b31 algorithms show good agreement throughout the rainrate range. Between 3 and 14 mm hr^{-1}, the 2a12
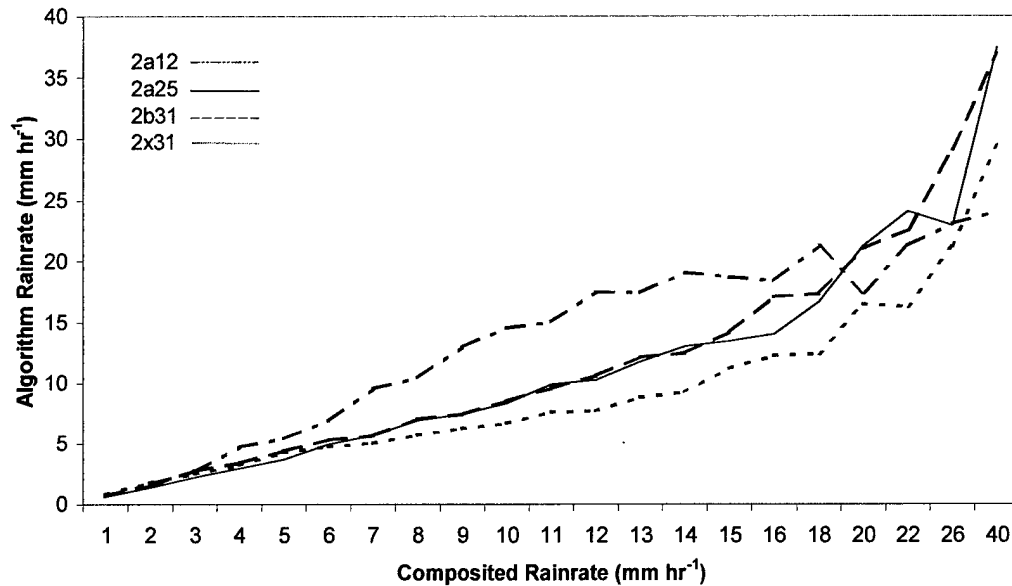
Figure 3: Algorithm-averaged surface rainrates vs composite rainrates.

graph exhibits the largest increase, growing by 660%, whereas 2x31 exhibits the smallest

increase at 268%, with 2a25 and 2b31 in between at a growth rate of 420%. However,

the 14 mm hr^{-1} data point marks the end of 2a12's rapid growth. After 14 mm hr^{-1}, the

2a25 and 2b31 algorithms indicate the largest rate of change, growing by 295% between

14 mm hr^{-1} near the end of the abscissa, while 2x31 indicates the next highest rate of

change at 220%, and 2a12 indicates the smallest rate of change growing by only 26%.

The 2a12 algorithm indicates the largest growth rate for this test, but this occurs

during the first half of the graph. Once into the higher rainrates, 2a12's rate of growth

decreases dramatically and becomes the algorithm with the lowest rate of growth.

Algorithms 2a25 and 2b31, the two algorithms most dependent on radar measurements,

indicate the largest rate of change for the higher rainrates, while 2x31, which also uses

radar measurements, indicates the next largest rate of change. This is consistent with the

31

expectations for the D^6 effect; the algorithms most dependent on the radar (2a25 and 2b31) exhibit the largest growth rate increase at high rainrates, while the tall vector combined algorithm (2x31), which is less dependent on radar measurements, exhibits a solid increase but not quite as large as for the two former algorithms. Therefore, the results of this test indicate that Hypothesis 2 is valid.

5.3 Test of Hypothesis 3

Figure 4 is a histogram of the 2a12/2a25 rain detection agreement skill score as a function of averaged surface rainrate. According to Hypothesis 3, the agreement skill score between the two algorithms should increase as the surface rainrate increases. The histogram shows that the agreement between the two algorithms at very low levels is indeed poor. For rainrates below 0.2 mm hr^{-1}, the agreement is less than 20%. However, the agreement skill score climbs quickly. Once rainrates exceed 0.4 mm hr^{-1}, the agreement skill score goes above 50%, where it stays along the remainder of the abscissa, occasionally reaching skill scores above 80%. There are a few skill scores dropping near 50% at rainrates of 14-16 mm hr^{-1}, but these are believed due to limited sampling of intense rainrates, more so than a deterioration of agreement skill scores at the higher rainrates. In any case, the results bear out the validity of Hypothesis 3.

5.4 Test of Hypothesis 4

Hypothesis 4 states that the 2a12 algorithm will have larger vertical differences between it and the other algorithms, than the other algorithms will have between themselves. This is due to the lack of vertical resolution in the TMI measurements. The first attempt to validate this hypothesis was inconclusive as noted above. Another
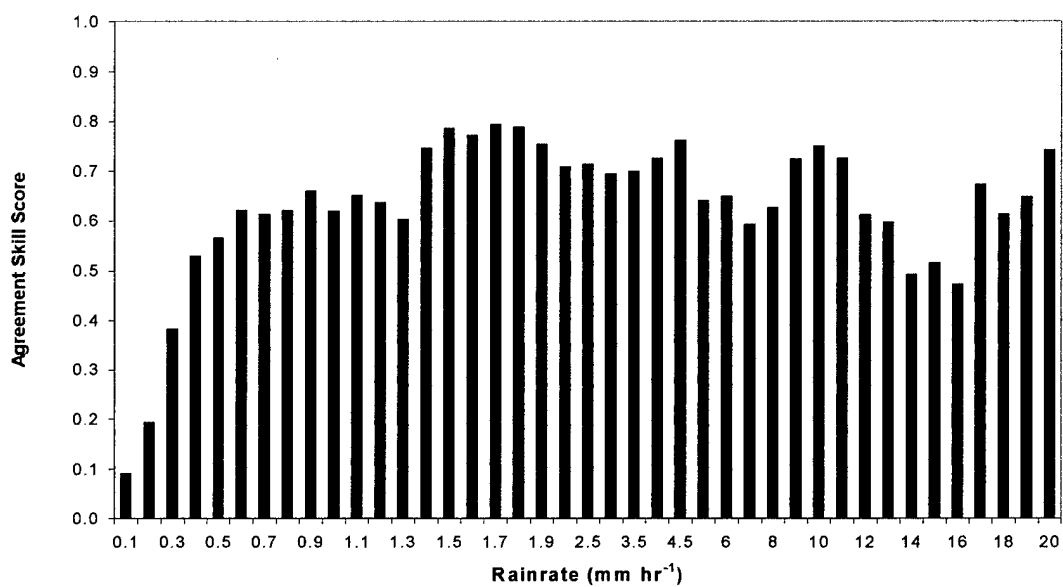
Figure 4: Histogram of 2a12/2a25 rain detection agreement skill score binned by averaged rainrate.
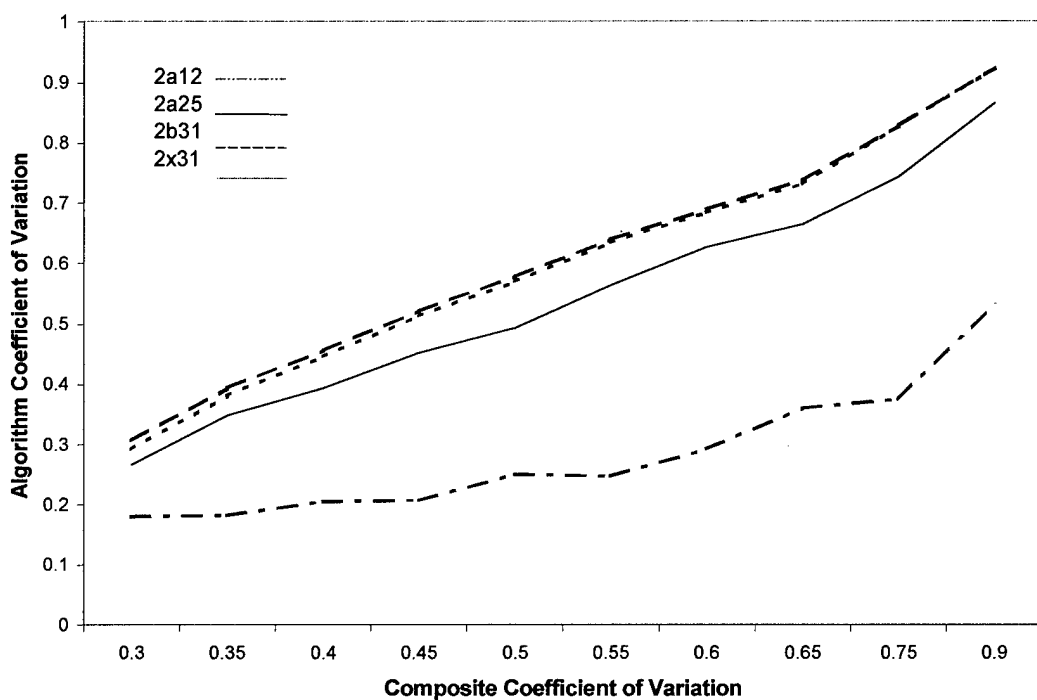
Figure 5: Algorithm coefficient of variation along vertical axis vs composite coefficient of variation for first six algorithm reporting levels.

33

attempt at validating Hypothesis 4 resulted in Figure 5, a diagram of the algorithm coefficient of variation with height graphed as a function of the composite coefficient of variation with height. Since the 2a12 algorithm's vertical resolution is limited by the TMI's broad weighting functions and fewer measurements along the vertical axis, it is expected that this algorithm would exhibit smaller variability along the vertical axis, or correspondingly a smaller coefficient of variation.

The Figure 5 diagram indicates that 2a12 does indeed have the smallest coefficient of variation. The 2a12 plot increases by less than 0.2 for a 0.45 change in the composite value. The 2a25 plot is next with an increase of 0.47 across the same interval. Finally, the plots for 2b31 and 2x31 are nearly identical indicating the largest increases at ~0.54, indicating that Hypothesis 4 is valid.

5.5 Test of Hypothesis 5

Hypothesis 5 states that 2a25 would differ more from the other algorithms as attenuation increases. The results of the test for this hypothesis are shown in Figure 6, with diagrams of the algorithm rainrates for the first four vertical levels graphed as functions of 10.7 GHz T_B. At first glance the test seems to have failed, with 2a12 indicating the greatest differences. While this is true behavior, 2a12's differences are not caused by attenuation alone. The major difference between 2a12 and the other algorithms is the result of the over estimated systematic differences between the Version 1 form of the 2a12 algorithm discussed above and expanded on in the study of Smith et al. (1999b). As noted, the Version 1 2a12 rainrate estimates are about 20% greater than the Version 1 estimates of the other algorithms.
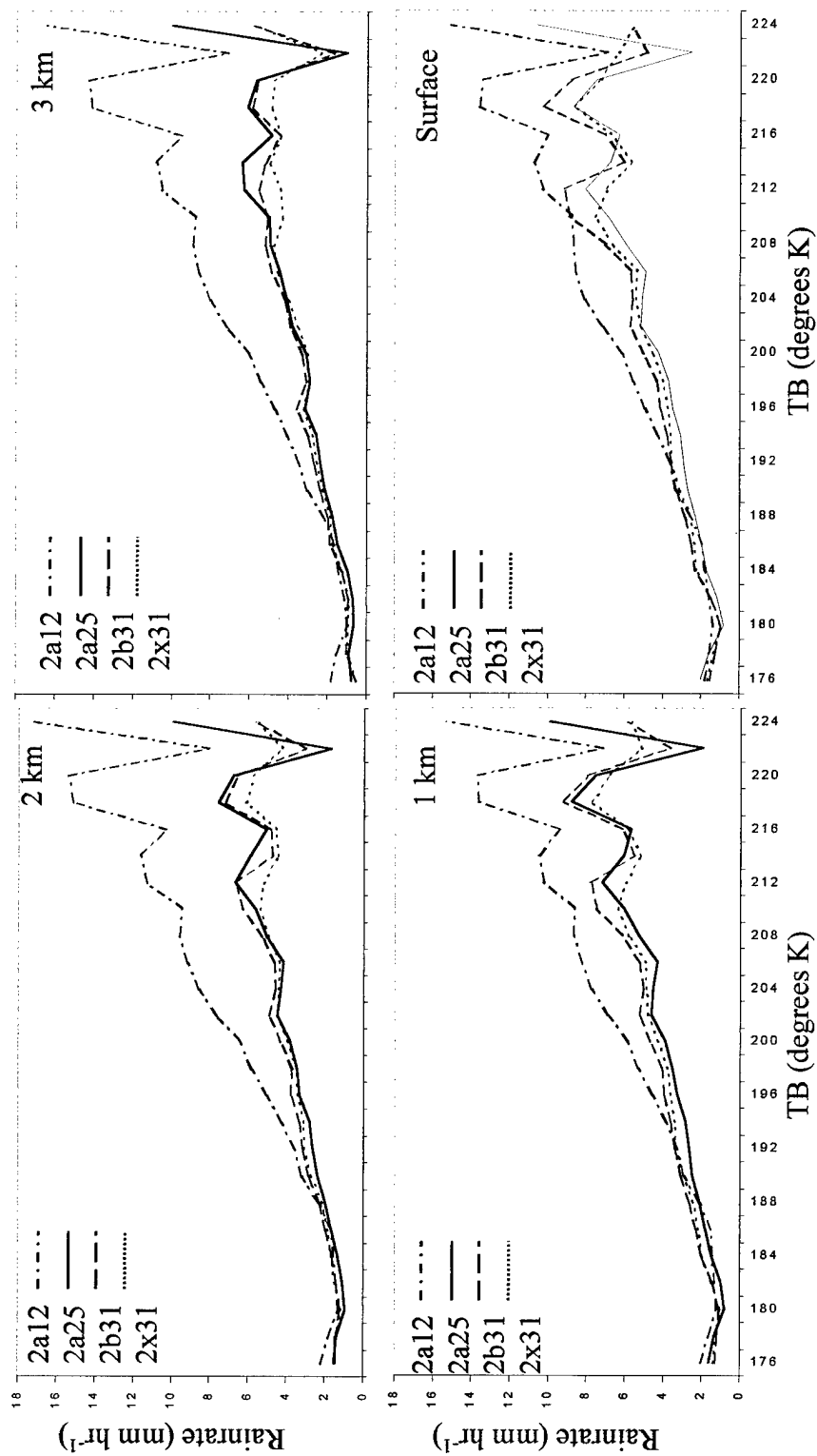
Figure 6: Algorithm averaged rainrates vs averaged 10-GHz TBs at four levels.

35

If only the other three algorithms are considered, the results adhere to the hypothesis. At all vertical levels the algorithms are in agreement, but with a change in the 2a25 algorithm's position relative to the other algorithms as the level decreases and the 10.7 GHz T_B increases. At all four levels the graphs of the 2a25 algorithm indicate the lowest rainrates at the lowest T_Bs, but at upper levels the 2a25 graphs increase to the highest rainrates at the higher T_Bs. At level 4, the increase begins around 198 K while at level 3 it begins around 206 K. By the time the 2nd level is reached, the 2a25 graph does not surpass the 2x31 graph until 210 K, and it surpasses the 2b31 graph only briefly between 213-215 K. At level 1, the 2a25 graph again surpasses the 2x31 graph at about 210 K, but sinks below it again at 216 K. They are nearly identical from 217-220 K, then 2a25 sinks below 2x31 again. The 2a25 graph also surpasses 2b31, but only from 213-215 K. As for the 2b31 and 2x31 graphs, they maintain the same relative position to each other for all four vertical levels.

In summary, the 2a25 graph has the same value relative to the other two algorithms at low T_Bs at all four vertical levels, but transitions from a greater relative value to a lesser value for the higher T_Bs as the level decreases. Meanwhile, 2b31 and 2x31 maintain their values relative to each other. This means that 2a25 is most influenced by attenuation, indicating Hypothesis 5 is valid.

While describing the algorithms in section 2, it was mentioned that 2b31 was derived from 2a25. If this is so, why is 2x31 not affected as much by attenuation as is algorithm 2a25? The answer is the difference in how each of the algorithms estimate PIA. The accuracy of a radar using attenuating frequencies is highly dependent on the accuracy of PIA estimates (Hitschfeld and Bordan, 1954). Algorithm 2a25 uses the SRT

36

as the final arbitrator for estimating PIA. This means that the PIA estimate is referenced to clear sky conditions based on a cloud-free surface reflectivity (σ_0) climatology (i.e., cloud-free σ_0s), not a σ_0 surface capped by heavy rainfall which may disturb the surface and diminish the reflectivity from a more mirror surface. By the same token, algorithm 2b31 uses 10.7 GHz T_Bs to estimate PIA over and above the SRT constraint (see Haddad et al., 1997). The result for 2b31 is an improved estimate of PIA and thus a better estimate of rainrate with less attenuation error.

5.6 Test of Hypothesis 6

Hypothesis 6 states that saturation of the higher TMI frequencies at higher rainrates would lead to better agreement between the two combined algorithms, 2b31 and 2x31. Figure 7 illustrates the algorithm-averaged surface rainrates for 2b31 and 2x31, graphed as a function of "restricted" composite surface rainrate (calculated from 2b31 and 2x31 alone). This diagram does not indicate convergence of the 2b31 and 2x31 graphs at the highest rainrates. However, a comparison of the graph slopes is revealing. From 5 mm hr^{-1} (where the graphs begin to diverge) to 14.5 mm hr^{-1}, the slope of 2b31 is 40% larger than the slope of 2x31 (1.14 and 0.82, respectively). From 14.5 mm hr^{-1}, where 2b31 begins its next slope change, to the end of the graph, the difference has dropped to 30% with 2b31 indicating a slope of 0.74 and 2x31 a slope of 0.57. Finally, from 17.5 mm hr^{-1}, where 2x31's slope changes to the end of the graph, the difference has dropped to only 10%, with 2b31's slope at 0.67 and 2x31's slope at 0.61. This reduction in the difference of slopes should be viewed as a partial success for the Hypothesis 6.
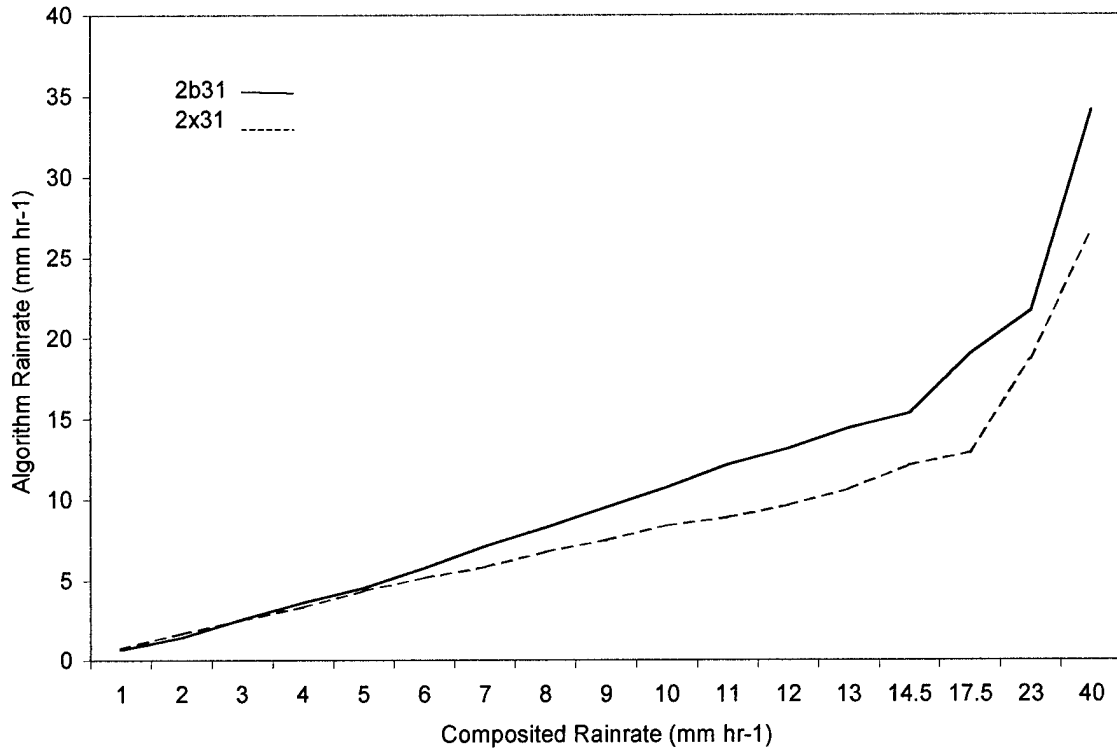
Figure 7: Algorithm-averaged rainrates (2b31 and 2x31 only) vs composite rainrates.

The reason Hypothesis 6 cannot be considered a complete success stems from the results of the Hypothesis 2 test. As noted, the 2b31 algorithm is more dependent on PR measurements than is the 2x31 algorithm (or perhaps less influenced by the TMI measurements as an alternate way to describe the basic difference). In that context, 2b31 is more influenced by the radar's D^6 effect. While the effect of cloud black body saturation in Hypothesis 6 is expected to lead to better agreement between 2b31 and 2x31 at higher rainrates, the greater influence of the D^6 effect on 2b31 stemming from Hypothesis 2, is reducing the expected agreement at higher rainrates under Hypothesis 6. It is important to note that at this juncture, there is no straightforward way to quantify the competing effects.
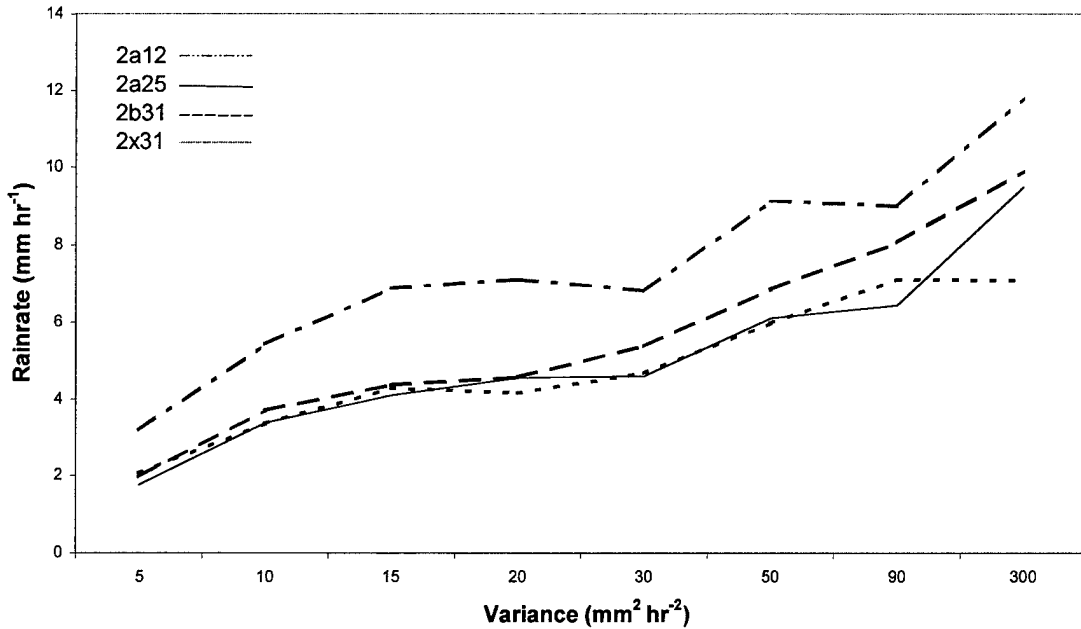
Figure 8: Algorithm-averaged rainrates vs variance of 2a25 storm feature rainrates.

5.7 Test of Hypothesis 7

Figure 8, a diagram of the algorithm-averaged surface rainrates graphed as a function of variance of the 2a25 surface rainrate for each storm feature, conveys the test of Hypothesis 7. This states that 2a12 should be most sensitive to beam filling heterogeneity. The diagram indicates that the 2a12 algorithm graph systematically exceeds those of the other algorithms. It climbs rapidly from 5-10 $mm^2\ hr^{-2}$, levels off between 15-30 $mm^2\ hr^{-2}$, then continues climbing along the remainder of the abscissa. However, the fluctuations of the 2a25 graph are nearly identical to those of the 2a12 graph, the 2a25 graph being slightly flatter between 10-30 $mm^2\ hr^{-2}$.

Clearly, the magnitudes of the 2a25 graph are smaller than those for 2a12. The graphs for the 2b31 and 2x31 algorithms do not track the 2a12 graph as well as 2a25, but the same overall patterns emerge. Thus the most salient feature of this diagram is the

39

systematically larger rainrates for algorithm 2a12. But these differences are anticipated and are related to the 2a12 Version 1 algorithm's systematic overestimation of ~20% as discussed previously. Therefore, putting aside the 2a12 differences in magnitude, this diagram does not exhibit any significant difference between any of the individual algorithm graphs. This means that the test results for Hypothesis 7 must be considered inconclusive.

CHAPTER 6

CONCLUSIONS

The purpose of this study was to seek verification of some existing methods of satellite precipitation estimation, as well as some newer combined methods that are possible for the first time, using radiometer and radar measurements from the recently launched TRMM satellite. The four level 2 TRMM facility rain profile algorithms under investigation, 2a12, 2a25, 2b31, and 2x31, are all physically based. Given the characteristics of the TMI and PR measurements and the governing assumptions used in designing the algorithms, seven well-founded hypotheses were formed concerning the expected performance of the algorithms relative to one another. After testing, it was found that: (1) the 2a12 algorithm is the most influenced by ice loading, as hypothesized; (2) 2a25 and 2b31, the algorithms most dependent on the influence of PR measurements, are also most affected by the underlying radar D^6 effect (with 2x31 affected to a lesser degree), as hypothesized; (3) rain detection agreement skill scores between 2a12 and 2a25 increase as storm rain intensity increases, as hypothesized; (4) vertical structure differences are greater between 2a12 and the other algorithms than between the other algorithms and themselves, as hypothesized; and (5) 2a25 is the algorithm most affected by path integrated attenuation, as hypothesized.

Testing of Hypothesis 6 concerning TMI's black body saturation effects, led to partial success. Although the results did not indicate 2b31 and 2x31 fully converging athigher rainrates as postulated, they did show strong decreases in the difference between the slopes of the 2b31 and 2x31 rainrate graphs. Since the saturation effect of Hypothesis 6 is offset by 2b31's increased sensitivity to the D^6 effect from Hypothesis 2, the decrease in the difference between the slopes of the rainrate graphs can be viewed as a conditional success for Hypothesis 6.

Finally, the test results for Hypothesis 7, concerning 2a12 beam filling uncertainty, were inconclusive. While 2a12 exhibits the greatest differences between itself and the other algorithms, there is not sufficient evidence to determine whether the differences are caused by beam filling effects or by the 20% systematic over estimation known to exist within the Version 1 2a12 rain retrievals.

Notwithstanding the results for Hypothesis 7, the results summarized above suggest that the four level 2 TRMM facility rain profile algorithms are performing within the limitations of the TMI and PR measurements, and according to the underlying physical assumptions used in the algorithm designs. Whereas some of the above interpretation of the hypothesis testing could be modified, our interpretation is consistent with the results of the tests as dictated by the hypotheses themselves, nothing more. It remains debatable whether our posed hypotheses are sufficiently complete and precisely enough formulated to fully defend the reliability of the TRMM level 2 facility algorithms.

In the area of precipitation retrieval, as in a number of other remote sensing areas, competition between algorithm producers runs high. Our emphasis here is to show that when the hierarchy of TRMM level 2 physical algorithms stemming from single

instrument to combined instrument are run together with controlled inputs, expected performance metrics can be quantitatively tested. In this respect, the results of our study offer solid evidence that the TRMM rain estimates are reliable within the context of the physics employed.

There is much more to be done in fully evaluating the accuracy and precision of the TRMM algorithms. Likely this can never be accomplished to the satisfaction of everyone using conventional ground truth schemes, and it remains a severe challenge to verify TRMM rain retrievals based on a precision "error model" that can serve as a calibration bench -- simply because developing such an error model is so overwhelming a project. A true error model would have to be capable of: (1) simulating near-exact 3-dimensional, non-steady state, and non-elastic radiative transport in complex and fluctuating gaseous-hydrometeor media (unconstrained by simplifying assumptions concerning hydrometeor shape, size distribution, orientation, and complex dielectric properties); (2) fully reproducing from first principles the emittance-reflectance properties of all varieties of natural earth surfaces over which rain falls; and (3) characterizing near-exact renditions of "real" precipitating clouds with nonhydrostatic 3-dimensional cloud models using fully explicit microphysical process models and capable of getting all the rest of the dynamics, thermodynamics, and hydrological processes of the atmosphere near perfect. That is a serious and possibly unachievable challenge, but the error model approach remains as the final arbitrator and final goal for satellite rain verification since we've nearly exhausted the accuracy and precision metrics attainable with established *in situ* measuring systems. Therefore we view these results as a "path" between ground truth comparison and classic error modeling. Also, the results also have a broader meaning. While the testing

methods used in this study cannot be used alone to quantify TRMM precipitation uncertainty in the conventional terms of accuracy and precision, they offer an independent means for corroborating other verification analyses. This is important considering that direct comparison methods have uncertainty problems of their own.

APPENDIX

The storms and storm features described in section 3.2 are all listed here in the appendix. Table 2 lists all the storms by number and gives the storm type, date, and time. If the storm was named, that name is listed under storm type. Table 3 also lists the storms by number but it lists the number of the TRMM swathe that contained the storm data and the location of the storm. The location is given by listing the maximum and minimum latitude and longitude. Finally, table 4 lists all the storm features for each storm and the minimum latitude and longitude for each feature. To get the maximum latitude and longitude, just add .3 to the minimum values.

Table 2. List of all storms by storm number, type of storm (name given if storm was named), date, and time.

Storm Number	Storm Type	Date	Time
1998_281_1352	Hurricane Lisa	8 October	1445
1998_281_1524	Cold Front	8 October	1650
1998_283_1303	Cold Front	10 October	1350
1998_284_0113	SPCZ	11 October	0235
1998_284_1758	Hurricane Zeb	11 October	1830
1998_285_0306	Hurricane Zeb	12 October	0410
1998_285_1043	ITCZ	12 October	1110
1998_288_0540	Trop Storm 05A	15 October	0642
1998_288_0712	ITCZ	15 October	0740
1998_288_1317	ITCZ	15 October	1420
1998_290_0623	Hurricane Lester	17 October	0650
1998_290_0700	Ex Trop Cyclone	17 October	0700
1998_290_0754	Hurricane Madeline	17 October	0825
1998_290_0925	ITCZ	17 October	0950

Table 2 (continued)

Storm Number	Storm Type	Date	Time
1998_290_1050	Ex Trop Cyclone	17 October	1015
1998_291_0512	Cold Front	18 October	0545
1998_291_1420	Hurricane Babs	18 October	1445
1998_292_0000	Hurricane Babs	19 October	0030
1998_292_0533	Cold Front	19 October	0615
1998_292_0600	Hurricane Lester	19 October	0600
1998_292_1310	ITCZ	19 October	1335
1998_292_1350	Cold Front	19 October	1350
1998_292_1610	ITCZ	19 October	1630
1998_292_1612	Cold Front	19 October	1650
1998_293_0554	ITCZ	20 October	0620
1998_293_1331	Hurricane Babs	20 October	1355
1998_293_1634	ITCZ	20 October	1735
1998_293_1650	ITCZ	20 October	1650
1998_294_1524	Cold Front	21 October	1605
1998_294_1545	ITCZ	21 October	1540
1998_295_0808	ITCZ	22 October	0910
1998_295_0940	Cold Front	22 October	0933
1998_296_0829	Cold Front	23 October	0925
1998_297_0245	Cold Front	24 October	0320
1998_297_0547	Cold Front	24 October	0635
1998_297_0710	Cold Front	24 October	0710
1998_297_1153	Cold Front	24 October	1235
1998_297_1324	Cold Front	24 October	1405
1998_298_1951	Hurricane Babs	25 October	2050
1998_299_0156	Ex Trop Cyclone	26 October	0235
1998_300_0046	Cold Front	27 October	0123
1998_300_0100	Hurricane Mitch	27 October	0115
1998_300_1125	Ex Trop Cyclone	27 October	1250
1998_301_0409	Ex Trop Cyclone	28 October	0500
1998_301_1015	Ex Trop Cyclone	28 October	1135
1998_303_0925	Ex Trop Cyclone	30 October	1010
1998_303_1000	ITCZ	30 October	0940
1998_304_0512	ITCZ	31 October	0615
1998_304_0644	Ex Trop Cyclone	31 October	0720

Table 3. List of all storm numbers, TRMM swath numbers, and locations given by maximum and minimum latitudes and longitudes.

Storm Number	Swathe Number	Max Lat	Min Lat	Max Lon	Min Lon
1998_281_1352	981008.4963	31.1° N	26.2° N	33.6° W	42.5° W
1998_281_1524	981008.4964	32.6° S	36.1°S	66.5°E	52.2°E
1998_283_1303	981010.4994	36.0°N	33.8°N	73.0°W	68.1°W
1998_284_0113	981011.5002	21.4°S	26.1°S	140.9°W	147.3°W
1998_284_1758	981011.5013	15.2°N	10.6°N	130.1°E	135.3°E
1998_285_0306	981012.5019	12.9°N	5.9°N	135.0°E	126.6°E
1998_285_1043	981012.5024	13.8°N	7.4°N	123.3°W	131.3°W
1998_288_0540	981015.5068	17.3°N	12.9°N	62.8°E	56.9°E
1998_288_0712	981015.5069	14.5°N	7.0°N	91.7°W	101.4°W
1998_288_1317	981015.5073	12.0°N	3.3°N	40.3°W	51.8°W
1998_290_0623	981017.5100	15.8°N	10.3°N	92.9°W	100.0°W
1998_290_0700	981017.5100	33.5°N	29.0°N	53.3°W	62.8°W
1998_290_0754	981017.5101	22.2°N	18.2°N	105.6°W	110.5°W
1998_290_0925	981017.5102	11.5°N	7.0°N	145.7°W	150.9°W
1998_290_1050	981017.5102	34.7°N	31.5°N	52.3°W	59.2°W
1998_291_0512	981018.5115	32.4°N	26.3°N	47.5°W	60.6°W
1998_291_1420	981018.5121	12.7°N	7.4°N	132.7°E	126.8°E
1998_292_0000	981019.5127	12.6°N	6.0°N	136.3°E	127.9°E
1998_292_0533	981019.5131	36.1°N	34.0°N	35.7°W	40.0°W
1998_292_0600	981019.5131	15.1°N	10.5°N	97.0°W	102.2°W
1998_292_1310	981019.5136	13.3°N	7.2°N	143.8°E	136.6°E
1998_292_1350	981019.5136	35.8°N	33.2°N	157.2°W	168.9°W
1998_292_1610	981019.5138	0.9°S	7.1°S	78.0°E	71.0°E
1998_292_1612	981019.5138	34.7°N	31.4°N	146.7°E	139.6°E
1998_293_0554	981020.5147	14.4°N	8.3°N	111.1°W	118.5°W
1998_293_1331	981020.5152	14.3°N	8.5°N	132.2°E	125.1°E
1998_293_1634	981020.5154	12.3°N	5.8°N	132.7°W	141.6°W
1998_293_1650	981020.5154	1.5°N	8.9°S	68.1°E	55.4°E
1998_294_1524	981021.5169	35.1°N	32.4°N	146.0°E	141.2°E
1998_294_1545	981021.5169	1.1°N	7.5°S	77.7°E	67.6°E
1998_295_0808	981022.5180	8.8°N	3.4°N	16.2°W	23.0°W
1998_295_0940	981022.5180	31.7°S	34.8°S	55.5°E	49.9°E
1998_296_0829	981023.5196	27.8°N	24.6°N	64.1°W	67.6°W
1998_297_0245	981024.5208	32.5°N	28.9°N	56.2°W	62.2°W
1998_297_0547	981024.5210	34.7°N	32.0°N	53.5°W	58.2°W
1998_297_0710	981024.5210	28.9°S	32.3°S	64.4°E	59.7°E
1998_297_1153	981024.5214	36.1°N	33.9°N	169.8°W	176.3°W

Table 3 (continued)

Storm Number	Swathe Number	Max Lat	Min Lat	Max Lon	Min Lon
1998_297_1324	981024.5215	34.7°N	31.1°N	151.2°E	142.7°E
1998_298_1951	981025.5235	22.8°N	18.3°N	118.9°E	113.0°E
1998_299_0156	981026.5239	34.2°N	29.7°N	51.6°W	62.6°W
1998_300_0046	981027.5254	32.5°N	29.5°N	49.0°W	52.9°W
1998_300_0100	981027.5254	20.9°N	15.0°N	76.1°W	84.8°W
1998_300_1125	981027.5261	30.2°S	33.6°S	39.4°W	45.4°W
1998_301_0409	981028.5272	31.3°N	27.2°N	42.9°W	49.9°W
1998_301_1015	981028.5276	29.0°S	32.4°S	34.4°W	39.7°W
1998_303_0925	981030.5307	36.1°N	33.8°N	179.8°E	172.7°E
1998_303_1000	981030.5307	6.4°S	11.8°S	89.2°E	83.1°E
1998_304_0512	981031.5320	9.3°N	1.4°N	38.7°W	48.9°W
1998_304_0644	981031.5321	35.1°N	29.3°N	158.7°W	176.0°W

Table 4. List of storm features for each storm and minimum latitude and longitude for each feature.

Storm Number	Feature Number	Min Lat	Min Lon
1998281_1352	1998281_1352_01	29.8°N	41.9°W
	1998281_1352_02	30.2°N	40.9°W
	1998281_1352_03	29.2°N	41.7°W
	1998281_1352_04	28.7°N	39.0°W
	1998281_1352_05	28.0°N	38.7°W
	1998281_1352_06	29.3°N	38.5°W
	1998281_1352_07	28.6°N	36.6°W
	1998281_1352_08	28.3°N	35.8°W
1998281_1524	1998281_1524_01	35.9°S	65.1°E
	1998281_1524_02	34.5°S	60.7°E
	1998281_1524_03	34.7°S	61.4°E
	1998281_1524_04	35.3°S	58.0°E
	1998281_1524_05	34.5°S	56.9°E
	1998281_1524_06	35.0°S	62.6°E
	1998281_1524_07	33.7°S	55.7°E
	1998281_1524_08	35.3°S	65.0°E
1998283_1303	1998283_1303_01	34.2°N	72.7°W
	1998283_1303_02	34.7°N	72.2°W
	1998283_1303_03	34.9°N	71.6°W
	1998283_1303_04	35.2°N	71.0°W

Table 4 (continued)

Storm Number	Feature Number	Min Lat	Min Lon
1998283_1303	1998283_1303_05	35.5°N	70.4°W
	1998283_1303_06	35.4°N	69.7°W
	1998283_1303_07	35.0°N	69.1°W
	1998283_1303_08	34.4°N	69.2°W
1998284_0113	1998284_0113_01	22.1°S	146.3°W
	1998284_0113_02	22.6°S	145.7°W
	1998284_0113_03	23.4°S	144.9°W
	1998284_0113_04	23.6°S	145.7°W
	1998284_0113_05	24.1°S	144.8°W
	1998284_0113_06	25.1°S	143.8°W
	1998284_0113_07	24.5°S	143.7°W
1998284_1758	1998284_1758_01	11.1°N	131.2°E
	1998284_1758_02	11.6°N	131.9°E
	1998284_1758_03	12.0°N	132.7°E
	1998284_1758_04	12.5°N	133.4°E
	1998284_1758_05	12.1°N	131.5°E
	1998284_1758_06	12.8°N	132.1°E
1998285_0306	1998285_0306_01	7.0°N	132.8°E
	1998285_0306_02	6.9°N	133.9°E
	1998285_0306_03	7.8°N	133.6°E
	1998285_0306_04	12.1°N	127.7°E
	1998285_0306_05	10.9°N	129.3°E
	1998285_0306_06	10.0°N	128.8°E
	1998285_0306_07	9.4°N	129.5°E
	1998285_0306_08	9.1°N	130.9°E
	1998285_0306_09	9.9°N	130.5°E
1998285_1043	1998285_1043_01	9.4°N	129.8°W
	1998285_1043_02	9.1°N	130.5°W
	1998285_1043_03	9.7°N	127.8°W
	1998285_1043_04	9.2°N	129.1°W
	1998285_1043_05	11.8°N	126.6°W
	1998285_1043_06	11.4°N	126.4°W
	1998285_1043_07	12.6°N	124.4°W
1998288_0540	1998288_0540_01	14.2°N	61.6°E
	1998288_0540_02	13.9°N	60.5°E
	1998288_0540_03	14.9°N	60.9°E
	1998288_0540_04	15.6°N	60.0°E
	1998288_0540_05	15.4°N	59.2°E
	1998288_0540_06	16.2°N	59.0°E

Table 4 (continued)

Storm Number	Feature Number	Min Lat	Min Lon
1998288_0540	1998288_0540_07	15.8°N	59.5°E
1998288_0712	1998288_0712_01	7.5°N	99.7°W
	1998288_0712_02	9.0°N	99.8°W
	1998288_0712_03	9.1°N	99.1°W
	1998288_0712_04	11.1°N	94.7°W
	1998288_0712_05	12.2°N	95.3°W
	1998288_0712_06	13.5°N	92.9°W
	1998288_0712_07	11.4°N	95.3°W
	1998288_0712_08	11.7°N	94.1°W
	1998288_0712_09	12.4°N	93.8°W
1998288_1317	1998288_1317_01	10.7°N	50.9°W
	1998288_1317_02	9.5°N	48.5°W
	1998288_1317_03	8.8°N	48.6°W
	1998288_1317_04	8.5°N	47.0°W
	1998288_1317_05	7.7°N	46.6°W
	1998288_1317_06	7.9°N	48.0°W
	1998288_1317_07	6.2°N	45.6°W
	1998288_1317_08	4.1°N	42.4°W
	1998288_1317_09	7.2°N	45.8°W
1998290_0623	1998290_0623_01	11.3°N	99.5°W
	1998290_0623_02	11.8°N	98.1°W
	1998290_0623_03	13.3°N	96.8°W
	1998290_0623_04	13.0°N	96.2°W
	1998290_0623_05	13.9°N	96.0°W
	1998290_0623_06	14.2°N	95.2°W
	1998290_0623_07	13.7°N	95.2°W
	1998290_0623_08	14.2°N	94.0°W
	1998290_0623_09	13.5°N	94.1°W
1998290_0700	1998290_0700_01	29.5°N	61.3°W
	1998290_0700_02	30.4°N	59.4°W
	1998290_0700_03	30.2°N	60.3°W
	1998290_0700_04	30.7°N	58.0°W
	1998290_0700_05	30.9°N	56.1°W
	1998290_0700_06	31.4°N	58.0°W
	1998290_0700_07	31.7°N	57.0°W
	1998290_0700_08	32.2°N	55.4°W
	1998290_0700_09	32.2°N	56.9°W
	1998290_0700_10	32.4°N	56.0°W
1998290_0754	1998290_0754_01	19.7°N	109.9°W

Table 4 (continued)

Storm Number	Feature Number	Min Lat	Min Lon
1998290_0754	1998290_0754_02	20.6°N	108.7°W
	1998290_0754_03	20.4°N	106.3°W
	1998290_0754_04	20.6°N	107.0°W
	1998290_0754_05	19.5°N	108.5°W
	1998290_0754_06	19.8°N	107.8°W
	1998290_0754_07	20.3°N	107.9°W
	1998290_0754_08	20.0°N	107.2°W
1998290_0925	1998290_0925_01	10.0°N	146.5°W
	1998290_0925_02	8.6°N	150.3°W
	1998290_0925_03	8.3°N	149.9°W
	1998290_0925_04	8.7°N	149.1°W
	1998290_0925_05	8.3°N	148.7°W
	1998290_0925_06	9.0°N	147.2°W
	1998290_0925_07	9.5°N	147.6°W
	1998290_0925_08	9.2°N	148.4°W
1998290_1050	1998290_1050_01	33.0°N	58.6°W
	1998290_1050_02	33.1°N	57.6°W
	1998290_1050_03	33.8°N	56.7°W
	1998290_1050_04	33.5°N	55.9°W
	1998290_1050_05	32.3°N	56.5°W
	1998290_1050_06	32.7°N	55.9°W
	1998290_1050_07	33.4°N	54.7°W
	1998290_1050_08	32.7°N	54.7°W
	1998290_1050_09	32.3°N	55.3°W
	1998290_1050_10	31.8°N	53.8°W
1998291_0512	1998291_0512_01	26.7°N	59.0°W
	1998291_0512_02	27.6°N	57.1°W
	1998291_0512_03	27.8°N	56.1°W
	1998291_0512_04	28.5°N	54.4°W
	1998291_0512_05	31.8°N	48.9°W
	1998291_0512_06	31.3°N	49.4°W
	1998291_0512_07	30.9°N	50.2°W
	1998291_0512_08	29.8°N	50.3°W
	1998291_0512_09	30.3°N	50.6°W
	1998291_0512_10	29.8°N	51.2°W
	1998291_0512_11	29.2°N	52.2°W
1998291_1420	1998291_1420_01	10.2°N	129.1°E
	1998291_1420_02	9.6°N	128.3°E
	1998291_1420_03	8.8°N	127.7°E

Table 4 (continued)

Storm Number	Feature Number	Min Lat	Min Lon
1998291_1420	1998291_1420_04	8.4°N	128.6°E
	1998291_1420_05	9.6°N	129.8°E
	1998291_1420_06	10.1°N	131.2°E
	1998291_1420_07	10.2°N	130.0°E
	1998291_1420_08	10.5°N	130.7°E
	1998291_1420_09	11.4°N	130.6°E
	1998291_1420_10	11.1°N	131.5°E
1998292_0000	1998292_0000_01	10.0°N	129.4°E
	1998292_0000_02	8.2°N	131.9°E
	1998292_0000_03	6.6°N	134.4°E
	1998292_0000_04	7.8°N	134.6°E
	1998292_0000_05	9.6°N	132.4°E
	1998292_0000_06	9.0°N	130.9°E
	1998292_0000_07	9.8°N	131.2°E
	1998292_0000_08	9.0°N	131.8°E
	1998292_0000_09	8.5°N	132.9°E
	1998292_0000_10	8.3°N	133.7°E
1998292_0533	1998292_0533_01	34.0°N	39.3°W
	1998292_0533_02	34.0°N	38.4°W
	1998292_0533_03	35.5°N	37.7°W
	1998292_0533_04	35.5°N	37.0°W
	1998292_0533_05	34.5°N	37.8°W
	1998292_0533_06	35.0°N	37.6°W
1998292_0600	1998292_0600_01	11.6°N	100.5°W
	1998292_0600_02	12.1°N	101.4°W
	1998292_0600_03	12.3°N	99.0°W
	1998292_0600_04	14.1°N	98.5°W
	1998292_0600_05	12.4°N	100.2°W
	1998292_0600_06	13.0°N	99.5°W
	1998292_0600_07	13.0°N	100.2°W
1998292_1310	1998292_1310_01	9.4°N	140.4°E
	1998292_1310_02	8.4°N	137.7°E
	1998292_1310_03	8.9°N	138.8°E
	1998292_1310_04	9.4°N	139.2°E
	1998292_1310_05	10.0°N	139.3°E
	1998292_1310_06	10.8°N	140.2°E
	1998292_1310_07	10.9°N	141.4°E
	1998292_1310_08	11.8°N	141.6°E
	1998292_1310_09	11.4°N	142.1°E

Table 4 (continued)

Storm Number	Feature Number	Min Lat	Min Lon
1998292_1310	1998292_1310_10	12.3°N	142.6°E
1998292_1350	1998292_1350_01	33.5°N	162.3°W
	1998292_1350_02	33.9°N	161.6°W
	1998292_1350_03	34.1°N	160.6°W
	1998292_1350_04	34.6°N	160.1°W
	1998292_1350_05	34.2°N	159.1°W
	1998292_1350_06	33.6°N	163.2°W
	1998292_1350_07	35.1°N	159.9°W
1998292_1610	1998292_1610_01	4.2°S	74.0°E
	1998292_1610_02	3.4°S	74.8°E
	1998292_1610_03	3.6°S	75.7°E
	1998292_1610_04	2.4°S	76.1°E
	1998292_1610_05	2.6°S	75.3°E
	1998292_1610_06	3.2°S	76.4°E
	1998292_1610_07	2.2°S	76.7°E
1998292_1612	1998292_1612_01	31.7°N	141.3°E
	1998292_1612_02	32.4°N	142.0°E
	1998292_1612_03	32.2°N	141.3°E
	1998292_1612_04	32.8°N	144.1°E
	1998292_1612_05	33.7°N	143.6°E
	1998292_1612_06	33.9°N	144.4°E
	1998292_1612_07	33.7°N	145.0°E
	1998292_1612_08	34.1°N	145.3°E
	1998292_1612_09	32.0°N	140.6°E
1998293_0554	1998293_0554_01	12.2°N	111.9°W
	1998293_0554_02	11.8°N	114.8°W
	1998293_0554_03	11.5°N	114.3°W
	1998293_0554_04	11.6°N	113.6°W
	1998293_0554_05	11.6°N	112.9°W
	1998293_0554_06	9.8°N	116.4°W
	1998293_0554_07	10.4°N	116.2°W
	1998293_0554_08	10.0°N	117.5°W
1998293_1331	1998293_1331_01	12.1°N	130.9°E
	1998293_1331_02	11.7°N	129.9°E
	1998293_1331_03	12.1°N	128.7°E
	1998293_1331_04	12.6°N	129.3°E
	1998293_1331_05	11.3°N	129.4°E
	1998293_1331_06	12.3°N	129.9°E
	1998293_1331_07	10.8°N	126.5°E

Table 4 (continued)

Storm Number	Feature Number	Min Lat	Min Lon
1998293_1331	1998293_1331_08	10.9°N	127.3°E
	1998293_1331_09	11.6°N	127.8°E
	1998293_1331_10	10.1°N	126.7°E
	1998293_1331_11	10.6°N	127.7°E
1998293_1634	1998293_1634_01	10.6°N	140.3°W
	1998293_1634_02	9.8°N	139.9°W
	1998293_1634_03	9.6°N	139.1°W
	1998293_1634_04	9.3°N	138.5°W
	1998293_1634_05	9.0°N	137.7°W
	1998293_1634_06	8.9°N	137.0°W
	1998293_1634_07	8.8°N	136.3°W
	1998293_1634_08	8.2°N	136.0°W
	1998293_1634_09	8.1°N	135.3°W
	1998293_1634_10	7.7°N	134.8°W
1998293_1650	1998293_1650_01	6.4°S	57.6°E
	1998293_1650_02	5.9°S	58.1°E
	1998293_1650_03	5.3°S	58.4°E
	1998293_1650_04	4.8°S	59.1°E
	1998293_1650_05	4.2°S	60.8°E
	1998293_1650_06	2.2°S	63.1°E
	1998293_1650_07	1.9°S	63.4°E
	1998293_1650_08	0.1°N	66.6°E
	1998293_1650_09	0.8°S	66.1°E
	1998293_1650_10	3.5°S	63.1°E
	1998293_1650_11	3.3°S	62.4°E
	1998293_1650_12	5.2°S	59.9°E
1998294_1524	1998294_1524_01	34.4°N	144.6°E
	1998294_1524_02	34.1°N	143.0°E
	1998294_1524_03	33.6°N	142.8°E
	1998294_1524_04	33.8°N	143.6°E
	1998294_1524_05	33.8°N	144.2°E
	1998294_1524_06	33.3°N	142.0°E
	1998294_1524_07	32.7°N	142.5°E
	1998294_1524_08	32.7°N	143.4°E
1998294_1545	1998294_1545_01	5.9°S	68.1°E
	1998294_1545_02	5.2°S	68.8°E
	1998294_1545_03	5.2°S	69.5°E
	1998294_1545_04	3.6°S	71.0°E
	1998294_1545_05	3.5°S	71.7°E

Table 4 (continued)

Storm Number	Feature Number	Min Lat	Min Lon
1998294_1545	1998294_1545_06	4.2°S	71.7°E
	1998294_1545_07	0.2°S	75.7°E
	1998294_1545_08	3.2°S	73.2°E
	1998294_1545_09	1.6°S	74.8°E
	1998294_1545_10	2.4°S	72.8°E
1998295_0808	1998295_0808_01	3.7°N	17.8°W
	1998295_0808_02	4.8°N	17.4°W
	1998295_0808_03	7.4°N	21.8°W
	1998295_0808_04	7.5°N	20.9°W
	1998295_0808_05	6.4°N	19.6°W
	1998295_0808_06	5.9°N	19.9°W
	1998295_0808_07	5.7°N	18.7°W
	1998295_0808_08	6.9°N	21.3°W
1998295_0940	1998295_0940_01	34.5°S	54.1°E
	1998295_0940_02	33.8°S	53.5°E
	1998295_0940_03	32.7°S	52.2°E
	1998295_0940_04	32.7°S	52.8°E
	1998295_0940_05	33.0°S	53.4°E
	1998295_0940_06	33.3°S	52.9°E
	1998295_0940_07	32.7°S	51.5°E
	1998295_0940_08	34.2°S	53.0°E
1998296_0829	1998296_0829_01	24.9°N	65.6°W
	1998296_0829_02	25.2°N	66.1°W
	1998296_0829_03	26.0°N	67.0°W
	1998296_0829_04	26.4°N	66.5°W
	1998296_0829_05	25.5°N	65.7°W
	1998296_0829_06	26.1°N	65.8°W
	1998296_0829_07	26.4°N	65.1°W
	1998296_0829_08	26.7°N	65.9°W
1998297_0245	1998297_0245_01	29.9°N	61.0°W
	1998297_0245_02	30.3°N	60.3°W
	1998297_0245_03	30.7°N	59.7°W
	1998297_0245_04	31.3°N	59.1°W
	1998297_0245_05	31.6°N	57.7°W
	1998297_0245_06	29.9°N	58.3°W
	1998297_0245_07	30.1°N	59.0°W
1998297_0547	1998297_0547_01	32.6°N	57.2°W
	1998297_0547_02	33.0°N	56.8°W
	1998297_0547_03	33.4°N	56.2°W

Table 4 (continued)

Storm Number	Feature Number	Min Lat	Min Lon
1998297_0547	1998297_0547_04	33.9°N	56.1°W
	1998297_0547_05	33.6°N	55.4°W
	1998297_0547_06	33.7°N	54.8°W
	1998297_0547_07	33.1°N	55.6°W
	1998297_0547_08	32.5°N	56.3°W
1998297_0710	1998297_0710_01	31.9°S	63.0°E
	1998297_0710_02	31.4°S	62.5°E
	1998297_0710_03	30.9°S	62.2°E
	1998297_0710_04	30.4°S	61.7°E
	1998297_0710_05	29.8°S	60.9°E
	1998297_0710_06	31.3°S	61.5°E
1998297_1153	1998297_1153_01	34.0°N	174.8°W
	1998297_1153_02	34.3°N	174.2°W
	1998297_1153_03	34.7°N	173.8°W
	1998297_1153_04	35.0°N	172.9°W
	1998297_1153_05	35.4°N	172.3°W
	1998297_1153_06	35.5°N	171.5°W
	1998297_1153_07	35.5°N	172.9°W
1998297_1324	1998297_1324_01	31.7°N	143.7°E
	1998297_1324_02	32.0°N	144.3°E
	1998297_1324_03	32.8°N	146.2°E
	1998297_1324_04	32.8°N	146.9°E
	1998297_1324_05	33.7°N	147.4°E
	1998297_1324_06	33.4°N	148.5°E
	1998297_1324_07	33.6°N	149.3°E
	1998297_1324_08	34.0°N	149.1°E
1998298_1951	1998298_1951_01	21.2°N	114.1°E
	1998298_1951_02	21.3°N	115.6°E
	1998298_1951_03	20.6°N	116.9°E
	1998298_1951_04	20.1°N	116.9°E
	1998298_1951_05	19.6°N	116.7°E
	1998298_1951_06	20.4°N	115.1°E
	1998298_1951_07	21.7°N	114.3°E
1998299_0156	1998299_0156_01	33.6°N	53.2°W
	1998299_0156_02	33.3°N	54.5°W
	1998299_0156_03	32.0°N	54.5°W
	1998299_0156_04	32.7°N	54.3°W
	1998299_0156_05	32.7°N	56.0°W
	1998299_0156_06	30.8°N	60.7°W

Table 4 (continued)

Storm Number	Feature Number	Min Lat	Min Lon
1998299_0156	1998299_0156_07	30.8°N	59.8°W
	1998299_0156_08	33.1°N	53.1°W
1998300_0046	1998300_0046_01	29.9°N	51.8°W
	1998300_0046_02	30.5°N	51.5°W
	1998300_0046_03	31.3°N	51.5°W
	1998300_0046_04	31.3°N	50.8°W
	1998300_0046_05	30.5°N	50.6°W
	1998300_0046_06	31.7°N	50.0°W
	1998300_0046_07	30.5°N	52.4°W
1998300_0100	1998300_0100_01	19.1°N	77.4°W
	1998300_0100_02	19.5°N	79.0°W
	1998300_0100_03	18.6°N	79.2°W
	1998300_0100_04	15.6°N	83.5°W
	1998300_0100_05	16.0°N	84.1°W
	1998300_0100_06	16.2°N	82.6°W
	1998300_0100_07	16.6°N	83.7°W
	1998300_0100_08	16.9°N	83.0°W
	1998300_0100_09	16.9°N	82.3°W
1998300_1125	1998300_1125_01	32.4°S	44.5°W
	1998300_1125_02	32.0°S	44.1°W
	1998300_1125_03	31.8°S	44.8°W
	1998300_1125_04	31.5°S	44.2°W
	1998300_1125_05	32.9°S	42.8°W
	1998300_1125_06	32.4°S	42.4°W
	1998300_1125_07	33.0°S	42.1°W
	1998300_1125_08	31.8°S	42.0°W
1998301_0409	1998301_0409_01	28.9°N	44.0°W
	1998301_0409_02	28.1°N	45.7°W
	1998301_0409_03	28.6°N	45.8°W
	1998301_0409_04	30.3°N	48.2°W
	1998301_0409_05	29.9°N	47.6°W
	1998301_0409_06	29.0°N	47.6°W
	1998301_0409_07	29.1°N	48.7°W
	1998301_0409_08	29.8°N	48.8°W
1998301_1015	1998301_1015_01	31.9°S	36.4°W
	1998301_1015_02	29.8°S	38.8°W
	1998301_1015_03	30.4°S	38.6°W
	1998301_1015_04	30.9°S	37.9°W
	1998301_1015_05	31.2°S	37.1°W

Table 4 (continued)

Storm Number	Feature Number	Min Lat	Min Lon
1998301_1015	1998301_1015_06	30.3°S	37.7°W
	1998301_1015_07	30.3°S	36.8°W
	1998301_1015_08	31.4°S	37.7°W
1998303_0925	1998303_0925_01	35.3°N	175.4°E
	1998303_0925_02	35.3°N	176.6°E
	1998303_0925_03	35.3°N	178.3°E
	1998303_0925_04	34.1°N	176.9°E
	1998303_0925_05	34.5°N	174.0°E
	1998303_0925_06	34.4°N	174.8°E
	1998303_0925_07	34.9°N	175.0°E
	1998303_0925_08	34.7°N	175.6°E
	1998303_0925_09	34.8°N	176.3°E
	1998303_0925_10	34.2°N	177.9°E
1998303_1000	1998303_1000_01	9.9°S	83.9°E
	1998303_1000_02	9.3°S	85.1°E
	1998303_1000_03	9.5°S	84.5°E
	1998303_1000_04	9.2°S	85.8°E
	1998303_1000_05	8.9°S	87.6°E
	1998303_1000_06	8.5°S	88.1°E
	1998303_1000_07	8.8°S	87.1°E
1998304_0512	1998304_0512_01	7.2°N	47.8°W
	1998304_0512_02	2.2°N	40.8°W
	1998304_0512_03	4.7°N	42.4°W
	1998304_0512_04	3.9°N	42.8°W
	1998304_0512_05	7.6°N	47.2°W
	1998304_0512_06	5.7°N	44.3°W
	1998304_0512_07	5.2°N	43.5°W
1998304_0644	1998304_0644_01	30.1°N	175.0°W
	1998304_0644_02	30.4°N	174.0°W
	1998304_0644_03	31.1°N	172.6°W
	1998304_0644_04	33.5°N	164.3°W
	1998304_0644_05	34.0°N	162.9°W
	1998304_0644_06	33.4°N	163.4°W
	1998304_0644_07	33.7°N	162.5°W
	1998304_0644_08	34.5°N	159.6°W

REFERENCES

Arkin, P. A., and B. Meisner, 1987: The relationship between large-scale convective rainfall and cold cloud over the Western Hemisphere during 1982-1984. *Mon. Wea. Rev.*, **115**, 51-74.

Barrett, E. C., and D. W. Martin, 1981: *The Use of Satellite Data in Rainfall Monitoring.* Academic Press, London, 340 pp.

Bell, T. L., A. Abdullah, R. L. Martin, and G. L. North, 1990: Sampling errors for satellite derived tropical rainfall: Monte Carlo study using a space-time stochastic model. *J. Geophys. Res.*, **95D**, 2195-2205.

Bellon, A., and G. L. Austin, 1986: On the relative accuracy of satellite and raingage rainfall measurements over middle latitudes during daylight hours. *J. Clim. Appl. Meteor.*, **25**, 1712-1724.

Damant, C., G. L. Austin, A. Bellon, and R. S. Broughton, 1983: Errors in the Thiessen technique for estimating areal rain amounts using weather radar data. *J. Hydrol.*, **62**, 81-94.

Dodge, J. C., and H. M. Goodman, 1994: The WetNet project. *Rem. Sens. Reviews*, **11**, 5-21.

Farrar, M.R., 1997.: Combined radar-radiometer rainfall retrieval for TRMM using structure function-based optimization. Ph.D. Dissertation, Dept. of Meteorology, Florida State University, Tallahassee, FL, 185 pp.

Farrar, M. R., E. A. Smith, Z. Haddad, and J. Turk, 1999: Combined radar-radiometer precipitation retrieval for TRMM. Part 2: A tall vector retrieval algorithm. *J. Appl. Meteor.*, submitted.

Gadgil, S., and S. Sajani, 1999: Monsoon precipitation in the AMIP runs. *Climate Dynamics*, accepted.

Haddad, Z. S., E. A. Smith, C. D. Kummerow, T. Iguchi, M. R. Farrar, S. L. Durden, M. Alves, and W. S. Olson, 1997: The TRMM 'Day-1' radar/radiometer combined rain-profiling algorithm. *J. Meteor. Soc. Japan*, **75**, 799-809.

Harrold, T. W., E. J. English, and C. A. Nicholass, 1973: The Dee weather radar project: The measurement of area precipitation using radar. *Weather,* **28**, 332-338.

Hitschfeld, W., and J. Bordan, 1954: Errors inherent in the radar measurement of rainfall at attenuating wavelengths. *J. Meteor.,* **11**, 58-67.

Hou, A. Y., D. Ledvina, A. da Silva, S. Zhang, J. Joiner, R. Atlas, G. Huffman, and C. Kummerow, 1999a: Assimilation of SSM/I-derived surface rainfall and total precipitable water for improving the GEOS analysis for climate studies. *Mon Wea. Rev.,* in press.

Hou, A. Y., S. Zhang, A. da Silva, and R. Rood, 1999b: Improving assimilated global data sets using SSM/I-derived precipitation and columnar moisture observations. *GEWEX News,* **9**, No. 1/February.

Iguchi, T., and R. Meneghini, 1994: Intercomparison of single-frequency methods for retrieving a vertical rain profile from airborne or spaceborne radar data. *J. Atmos. Oceanic Tech.,* **11**, 1507-1511.

Kummerow, C., W. S. Olson, and L. Giglio, 1996: A simplified scheme for obtaining precipitation and vertical hydrometeor profiles from passive microwave sensors. *IEEE Trans. Geosci. Rem. Sens.,* **34**, 1213-1232.

Kummerow, C., W. Barnes, T. Kozu, J. Shiue, and J. Simpson, 1998: The Tropical Rainfall Measuring Mission (TRMM) sensor package. *J. Atmos. Oceanic Tech.,* **15**, 809-817.

Meneghini, R.J., J. Eckerman, and D. Atlas, 1983: Determination of rain rate from a spaceborne radar technique. *IEEE Trans. Geosci. Rem Sens.,* **21**, 34-43.

Morrissey, M. L., 1991: Using sparse raingages to test satellite-based rainfall algorithms. *J. Geophys. Res.,* **96**, 18561-18571.

Mugnai, A., H. J. Cooper, E. A. Smith and G. J. Tripoli, 1990: Simulation of microwave brightness temperatures of an evolving hail storm at the SSM/I frequencies. *Bull. Amer. Meteor. Soc.,* **71**, 2-13.

Panegrossi, G., S. Dietrich, F. S. Marzano, A. Mugnai, E. A. Smith, X. Xiang, G. J. Tripoli, P. K. Wang, and J. P. V. Poiares Baptista, 1998: Use of cloud model microphysics for passive microwave-based precipitation retrieval: Significance of consistency between model and measurement manifolds. *J. Atmos. Sci.,* **55**, 1644-1673.

Rodriguez-Iturbe, I., and J. M. Mejia, 1974: The design of rainfall networks in time and space. *Water Resour. Res.,* **10**, 713-728.

Seed, A., and G. L. Austin, 1990: Variability of summer Florida rainfall and its significance for the estimation of rainfall by gages, radar, and satellite. *J. Geophys. Res.*, **95D**, 2207-2215.

Shin, K. –S., and G. R. North, 1988: Sampling error study for rainfall estimate by satellite using a stochastic model. *J. Appl. Meteor.*, **28**, 1218-1231.

Simpson, J., R. F. Adler, and G. R. North, 1988: A proposed Tropical Rainfall Measuring Mission (TRMM) satellite. *Bull. Amer. Meteor. Soc.* **69**, 278-295.

Simpson, J., and C. Kummerow, 1996: TRMM Science Operations Plan. TRMM Home Page, NASA/Goddard Space Flight Center, Greenbelt, MD, http://www.trmm.gsfc. nasa.gov.

Simpson, J., C. Kummerow, W. –K. Tao, and R. F. Adler, 1996: On the Tropical Rainfall Measuring Mission (TRMM). *Meteorol. Atmos. Phys.* **60**, 19-36.

Smith, E.A., X. Xiang, A. Mugnai, and G. Tripoli, 1992: A cloud radiation model for spaceborne precipitation retrieval. Extended Abstract Vol. of International TRMM Workshop on the Processing and Utilization of the Rainfall Data Measured from Space, Communications Research Laboratory, Tokyo, Japan, 273-283.

Smith, E. A., X. Xiang, A. Mugnai, and G. J. Tripoli, 1994a: Design of an inversion-based precipitation profile retrieval algorithm using an explicit cloud model for initial guess microphysics. *Meteorol. Atmos. Phys.*, **54**, 53-78.

Smith, E. A., C. Kummerow, and A. Mugnai, 1994b: The emergence of inversion-type profile algorithms for estimation of precipitation from satellite passive microwave measurements. *Remote Sensing Reviews,* **11**, 211-242.

Smith, E. A., A. Mugnai, and G. Tripoli, 1995a: Theoretical foundations and verification of a multispectral, inversion-type microwave precipitation profile retrieval algorithm. In *Passive Microwave Remote Sensing of Land-Atmosphere Interactions* (599-621), VSP Press, Utrecht - The Netherlands, 685 pp.

Smith, E. A., Z. Haddad, and C. Kummerow, 1995b: Overview on TRMM combined algorithm development. Contribution to TRMM Science Operations Plan (J. Simpson & C. Kummerow, eds.), Florida State University, Tallahassee, FL, 65 pp.

Smith, E. A., F. J. Turk, M. R. Farrar, A. Mugnai, and X. Xiang, 1997: Estimating 13.8-GHz path-integrated attenuation from 10.7-GHz brightness temperatures for the TRMM combined PR-TMI precipitation algorithm. *J. Appl. Meteor.*, **36**, 365-388.

Smith, E.A., J. Lamm, R. Adler, J. Alishouse, K. Aonashi, E. Barrett, P. Bauer, W. Berg, A. Chang, R. Ferraro, J. Ferriday, S. Goodman, N. Grody, C. Kidd, D. Kniveton, C. Kummerow, G. Liu, F. Marzano, A. Mugnai, W. Olson, G. Petty, A. Shibata, R.

Spencer, F. Wentz, T. Wilheit, and E. Zipser, 1998: Results of WetNet PIP-2 project. *J. Atmos. Sci.,* 55, 1483-1536.

Smith, E. A., M. R. Farrar, and X. Xiang, 1999a: Combined radar-radiometer precipitation retrieval for TRMM. Part 1: A unified RTE model for active and passive radiative transfer calculations. *J. Appl. Meteor.,* submitted.

Smith, E. A., S. Yang, A. Chang, Z. Haddad, Y. Hong, C. Kummerow, T. Iguchi, and T. Wilheit, 1999b: Intercomparison of Day One TRMM facility precipitation algorithms. *J. Appl. Meteor.,* in preparation.

Tao, W.-K., and J. Simpson, 1993: Goddard Cumulus Ensemble model. Part I: Model description. TAO, **4**, 35-72.

Tao, W. -K., S. Long, J. Simpson, and R. Adler, 1993a: Retrieval algorithms for estimating the vertical profiles of latent heat release: Their applications for TRMM. *J. Meteor. Soc. Japan,* **71**, 685-700.

Tao, W. -K., J. Simpson, C. -H. Sui, B. Ferrier, S. Lang, J. Scala, M. -D. Chou, and K. Pickering, 1993b: Heating, moisture, and water budgets of tropical and midlatitude squall lines: Comparison and sensitivity to longwave radiation. *J. Atmos. Sci.,* **50**, 673-690.

Tripoli, G. J., 1992a: A nonhydrostatic model designed to simulate scale interaction. *Mon. Wea. Rev.,* **120**, 1342-1359.

Tripoli, G. J., 1992b: An explicit three-dimensional nonhydrostatic numerical simulation of a tropical cyclone. *Meteorol. Atmos. Phys.,* **49**, 229-254.

Wilheit, T., R. Adler, S. Avery, P. Bauer, W. Berg, A. Chang, J. Ferriday, N. Grody, S. Goodman, C. Kidd, D. Kniveton, C. Kummerow, A. Mugnai, W. Olson, G. Petty, A. Shibata, and E. Smith, 1994: Algorithms for the retrieval of rainfall from passive microwave measurements. *Remote Sensing Reviews,* **11**, 163-194.

Yang, S., and E. A. Smith, 1999a: Moisture budget analysis of TOGA-COARE area using SSM/I retrieved latent heating and large scale Q_2 estimates. *J. Atmos. Oceanic Technol.,* in press.

Yang, S., and E. A. Smith, 1999b: Four dimensional structure of monthly latent heating derived from SSM/I satellite measurements. *J. Clim.,* **12**, 1016-1037.

Yang, S., and E.A. Smith, 1999c: Vertical structure and transient behavior of convective-stratiform heating in TOGA-COARE from combined satellite-sounding analysis. *J. Appl. Meteor.,* accepted.

BIOGRAPHICAL SKETCH

Throy Hollis was born in Abilene, Texas and raised in Louisiana. He graduated high school from Anacoco High School in 1982 and immediately joined the Air Force. While stationed at Offutt AFB began attending college at the University of Nebraska at Omaha in the fall of 1988. He obtained an associate's degree from the Community College of the Air Force in the spring of 1991. Throy was accepted into the Air Force's Airman's Education and Commissioning Program in August 1991 and transferred to Florida State University for classes in the spring semester of 1992. He received a bachelor of science degree in meteorology from Florida State in April 1994. Three years later he was selected for the Air Force Institute of Technology civilian institution program and returned to Florida State, where he is currently pursuing a master's degree in meteorology.